Università degli Studi di Padova

Dipartimento di Fisica e Astronomia
"Galileo Galilei"

Corso di Laurea Magistrale in Fisica

Effective long-range interactions and active flocking: the role of boundary conditions.

Relatori:
Prof. Enzo Orlandini
Dr. Fulvio Baldovin

Laureando:
Davide Colì

Anno Accademico: 2014/2015

"Curiously enough, the only thing that went through the mind of the bowl of petunias as it fell was «Oh no, not again.». Many people have speculated that if we knew exactly why the bowl of petunias had thought that, we would know a lot more about the nature of the Universe than we do now."

Douglas Adams, `The Hitchhiker's Guide to the Galaxy`

Abstract

The study of systems composed by active particles has become an important research topic in the last decade. In Statistical Mechanics it raises questions about non-equilibrium phase transitions since active particles are endowed with internal free energy depot which keep themselves out-of-equilibrium and, when interacting, can generate collective motion (flocking) and dynamical aggregation (clustering). Many diverse models, implementing the basic ingredients which allow collective motion, have been proposed in order to capture the global features displayed by these active systems. However a sufficiently wide and predictive model has yet to be found. In this thesis we study a continuous time model for the description of a two-dimensional coherent motion in groups of locally interacting biological units, based on the well established Vicsek model . We examine this system, in analytical and numerical fashions, in domains with different boundary conditions. We show that changing such boundary conditions dramatically influences the properties of particles dynamics. With reflecting boundary conditions in a static disk, typically a rotating behaviour along the border arises. While, with a moving disk confinement a much richer phenomenology occurs.

CONTENTS

INTRODUCTION

An interesting aspect of biological matter is the capability of transducing internal replenishable energy depot into useful work. This property may be seen as the defining characteristic of active matter [1]. Since active particles can move even in the complete absence of external forces, they are generally referred to as *self-propelled particles*. Examples of active matter can be found at many scales. At the smallest scale, there are molecular motors, i.e. protein complexes that harness the chemical free energy, generally released by ATP hydrolase, into mechanical work. On a larger scale there are living motile organisms, such as cells or bacteria, which can perform, thanks to the presence of cilia or flagella, complicated deformations of their body that permit them to move in fluids. Finally on even larger scale, we have many kinds of living organisms, such as birds, fishes, humans, or even man-made systems like queueing vehicles and self-organising mobile robots.

Active particles may interact both directly or through disturbances propagated via the medium in which they are immersed (e.g. chemotaxis). These interactions lead to remarkable collective behaviours, separated by non-equilibrium phase transitions between dynamical phases. One of the most common example of collective behaviour, shown by biological units, is the formation of flocks, e.g. large aggregations of animals moving altogether. Such a behaviour is generally observed in flocks of birds, school of fishes, swarms of insects or herds of mammal. However, there are examples of similar phenomena at smaller scales in systems composed by bacteria [2], sperm cells [3], mixtures of microtubules and molecular motors [4]. We will generally refer to this phenomenon as *flocking*. Beyond the complexity of each particular system, common features [5] causing the emergence of long-range order seem to point out the existence of some universal behaviour. This, in turn, makes it possible to attempt studying swarm motion using simple models.

Historically, the first flocking model developed is the so called Vicsek model [6]. While being minimal and simple, it still predicts the emergence of typical dynamical behaviours observed in flocks, such as particles gathering in small groups and moving altogether towards a certain direction. Later, several more complex models have been developed, however Vicsek model still plays a central role for its minimal character and the capability to produce motions qualitatively similar to some empirical observations [7].

Thesis Aims. In this thesis we aim at developing an analytical model, based on the Vicsek Model, in order to study the flocking behaviour of a two-dimensional system of self-propelled particles. Our guiding line is that by studying such model, we can receive information on the minimal feature needed by a flocking model to correctly predict the variety of dynamical patterns observed in nature. We will use both analytical and numerical means to examine our model in domains with different boundary conditions.

In chapter 1, at first we will describe some of the flocking models studied in the recent years. Later we will develop a continuous time version of the Vicsek model and investigate it analytically, mapping it into the so called *Hamiltonian Mean Field* model which deals with XY-spins with long-range interactions. Lastly we study our model in a domain with periodic boundary conditions, comparing numerical and analytical results.

In chapter 2 we will study our model in a domain restricted by a static disk with reflecting boundaries conditions at the border. We will employ analytical tools to prove the existence of a rotating steady state which is observed in numerical simulations.

In chapter 3 we will study our model in a domain where particles are confined inside a moving disk centred in the centre of mass of the particles. Numerical simulations show that this systems can give rise to a variety of realistic patterns.

CHAPTER 1

FLOCKING MODELS

1.1 COLLECTIVE ACTIVE MOTION

To correctly describe the dynamics of a living system, we must take into account the microscopic internal structure of its components and their dynamics. However, such approach is not ideal, since it would imply taking into account a huge number of degrees of freedom. In physics indeed we usually employ a coarse-grained description of such a system, neglecting the internal dynamics. Henceforth, in this approach, dynamics of a living system can not be completely described by the usual laws of Hamiltonian mechanics. Living systems are therefore studied considering their internal source of energy which allows autonomous motion. Thus, we can conclude that self-propulsion is a universal feature, displayed by living systems. Actually, this feature can be found in even more elementary systems, like active colloids [8], anisotropic vibrated rods [9] and molecular motors[10]. Henceforth, we will generally call *self-propelled particle* each object displaying internal degrees of freedom, regardless of its actual nature.

When we have large aggregations of self-propelled particles, phenomena of collective behaviours can arise. Particularly interesting is the case when aggregations self-organise into complex patterns, with apparently no need of an external stimulus. A typical example of this can be observed even in everyday life, such as when birds, for no evident reason, start flying in complex patterns and eventually form a compact flock. If we examine this system in details, we can find a number of possible relevant properties, such as birds dimensions, their range of vision, their speed, etc. At the current state of art, it is not clear which of these properties are fundamentals and needed in order to define a sufficiently wide and, at the same time, predictive model. This problem is surely common with almost any other self-propelled particles system. However, we can identify a class of systems, which show similar phenomenology, e.g. groups of birds forming a flock, fish forming schools or, even, collective migration of cell to repair a tissue [11]. A physical approach will therefore aim at identifying the minimal ingredients indispensable to produce a specific collective motion, identified in terms of its the common patterns (or phases) they give rise to.

Examples of collective motion patterns can be observed at every length scale. Bacteria, for example, show rotating patterns in confined domains [12], or display a growth in fractal patterns in stressed environments[13].This phenomenology is presumed to arise as a consequence of mutual long range interactions, mediated, for examples, by chemical signals released by the biological units (chemotaxis). At higher scales the most evident examples of collective motion are given by the already mentioned flocking phenomena, which can be observed in birds, mammals or even humans. We remark that, even if the individual behaviour of a bird or a human, seems to be more intricate than the one showed by a bacterium, the action of large groups of individuals, regardless of their biological complexity, display common patterns.

Flocks are characterised by a strong spatial coherence and can perform very fast and highly synchronised movements, either spontaneously, or as a response to external stimuli, such as predator attacks or turbulence. Empirical observations point out the existence of at least two universal minimal feature, which have to be included in a physical model describing such phenomenon. First, every unit move at almost the same speed. Secondly, units must either interact with their neighbours within a given range; such interactions have to, at least, include a component which favours an effective alignment between neighbours.

In recent years several flocking models has been developed, each of them often employs a different interaction form from the others. However, they have some common features we schematise below:

1. *Metric Interactions*. Each particle interacts with all the other particles within a certain range. Such kind of interaction closely resembles the ones used in classical mechanics. Some complex models, employing a metric interaction, are often based on a *behavioural zones* scheme [14], as displayed in fig. 1.1, where each zone is associated to a different conduct:

   (a) short range *repulsion zone*, the focal animal will seek to distance itself from its neighbours to avoid collision;
   (b) medium range *alignment zone*, the focal animal will seek to align its direction of motion with its neighbours;
   (c) long range *attraction zone*, the focal animal will seek to move towards a neighbour.

   Some models implement, an additional behavioural zone:

   (d) blind zone, the focal animal can not interact with units behind his back.

2. *Topological Interaction*. Each particle interacts with the other n_c nearest individuals regardless of their actual distance. n_c is a fixed number and it is often called *topological range*. We can have two possible kinds of topological interaction:

   (a) *Aligning* topological interactions; each particle will seek to align its direction with its nearest neighbours.

(b) *Attractive* topological interactions; particles will attract each other, regardless of their actual distance.

In this work we would like to find the minimal features needed by a model in order to implement a realistic flocking model. Our starting point is the so called Vicsek model [6], which takes into account only the existence of zone 1b. Vicsek model is therefore one of the simpler models we can use, but it still produces realistic results and a several dynamical patterns.

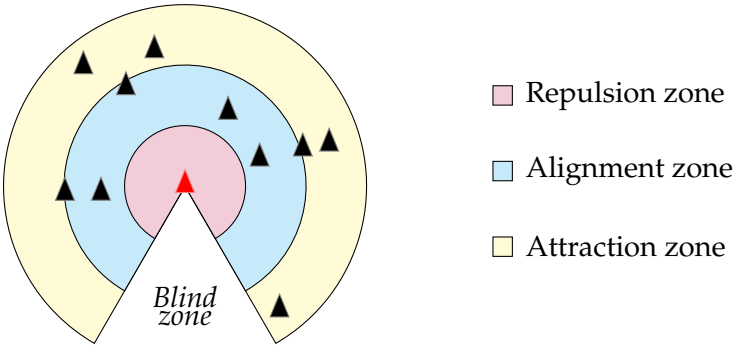

Figure 1.1: An illustrative diagram displaying the arrangement of the behavioural zones around a unit.

1.2 THE VICSEK MODEL

Vicsek model [6] is perhaps the simplest physical model proposed to describe the flocking behaviour of large groups of living organisms such as birds, fishes or bacteria. At each time-step every particle assume the average direction of motion of the particles in its neighbourhood, respecting the feature 1b in section 1.1. Furthermore, each particle moves at constant speed v_0, modelling the tendency of all units to move at almost the same speed. Note that particles do not attract (feature 1c), nor repel (feature 1b) each other.

Motion takes place in a two-dimensional plane, while time evolution is computed at a discrete pace Δt. We have N point-like particles; each particle i interacts with their neighbour particles within a circle $\mathcal{S}_R^{(i)}$ of radius R and thus we can identify Vicsek model as a *metric* model. Particles dynamics is described by the following equations:

$$\begin{cases} x_i(t+\Delta t) = x_i(t) + v_0 \cos(\theta_i(t))\Delta t & \text{(1.1a)} \\ y_i(t+\Delta t) = y_i(t) + v_0 \sin(\theta_i(t))\Delta t & \text{(1.1b)} \\ \theta_i(t+\Delta t) = \frac{1}{N_R^{(i)}} \sum_{\vec{x}_j \in \mathcal{S}_R^{(i)}} \theta_j(t) + \eta \Delta_i(t) & \text{(1.1c)} \end{cases},$$

where $\vec{x}_i = (x_i, y_i)^t$ is the position of i-th particle ($i = 1 \dots N$), θ_i is the velocity direction, N_R is the number of particles inside $\mathcal{S}_R^{(i)}$. $\Delta_i(t)$ is a random number chosen with a

uniform probability from the interval $[-\pi, \pi]$, while η is a constant in the interval $[0, 1]$ denoting the amount of noise affecting the system.

Stochastic noise is needed to modelise all possible, not predictable, disturbance in the motion, not considered in the model. Disturbance can have all kind of sources, both externals (possible interactions with the environment) and internal (erroneous decision making of the individual). However, there are several, not equivalent, ways to implement noise in Vicsek model. Indeed, different realisation of stochastic noise can lead to substantial difference in dynamics [15], which will be discussed later in this section. One of the possibility to implement noise is the original approach of Vicsek [6], already displayed in eq. (1.1). This implementation of the noise in the system is usually called *scalar* or *intrinsic* noise. It describes a situation where, at each step, each particles perfectly calculate the new direction of motion, but make an error when trying to take it because of unfavourable environment conditions. One can also think that the main source of errors is not the environment, but rather the imperfect interaction between particles [16]. This leads to change (1.1c) into:

$$\theta_i(t + \Delta t) = \theta_i(t + \Delta t) = \frac{\alpha}{N_R^{(i)}} \sum_{\vec{x}_j \in \mathcal{S}_R^{(i)}} \theta_j(t) + \beta \Delta_i(t) \ ; \tag{1.2}$$

where α and β are two positive numbers such that $\alpha + \beta = 1$. This kind of noise is often called *vectorial* or *extrinsic*.

In order to monitor the collective behaviour of the particles, we define the velocity magnetisation m as:

$$m = \left\| \frac{1}{N v_0} \sum_{i=1}^{N} \vec{v}_i \right\| \ , \tag{1.3}$$

where $\vec{v}_i$ stand for the velocity of the i-th particle. With $m = 1$ particles are moving all together in the same direction, while with $m = 0$ the particles display a motion with an incoherent direction. Note that such parameter is analogue to the ones used in spin models, e.g. with ferromagnetic interactions. Simulations, with a large number of particles (typically $N \gtrsim 10^3$) and fixed particle density $\rho = \frac{N}{L^2}$, show that the existence of a dynamical phase transition. At low noise levels η, particles form small clusters locally moving together ($m > 0$). Instead, at high noise levels particles motion orientations become incoherent and motion displays no ordered pattern ($m = 0$). The nature of this transition has been extensively studied and has been quite controversial. Some works, including the original one [6], claimed that the system has a continuous phase transition, while others [16] argued that it is a first order one. The solution has only been found recently [15]: the order of the phase transition is strongly dependent on the kind of noise (*scalar* or *vectorial*) employed. With a scalar noise, the phase transition is found to be continuous, while, with a vectorial noise, the transition is of the first order.

The spatial dynamic is strongly influenced by the far from equilibrium character of the system. At intermediate noise amplitude, not large enough to leave the ordered phase, the dynamics is characterised by the emergence of high-density moving bands [17]. To better study this phenomenon, it is useful to consider a system of particles

moving in a domain with periodic boundary conditions. We study an a arbitrary fraction A of this domain and examine the fluctuations of the number of particles contained in it. If we call $N^{(A)}(t)$ the number of particles in our region, we can define the parameter:

$$\Delta N^{(A)}(t) = \langle \left[N^{(A)}(t) - \langle N^{(A)} \rangle \right]^2 \rangle \quad . \tag{1.4}$$

In systems at equilibrium, we usually have that $\Delta N^{(A)}(t) \sim N^{(A)}(t)^{\frac{1}{2}}$, but in the Vicsek model, instead, we have that $\Delta N^{(A)}(t) \sim N^{(A)}(t)^{0.8}$ resulting in higher density fluctuations. Such phenomenon, usually referred to as *giant number fluctuations*, has been experimentally observed in several active systems, among which bacteria colonies [18] and agitated mono-layers of rods [19].

In conclusion, Vicsek model is central in the study of system presenting collective motion, because of its minimal character and because it can be easily extended [7]. For example, in this model particles do not maintain the spatial cohesion of a moving group: if the particles evolve in an infinite domain, they will eventually fly apart. Therefore, we could modify equations (1.1) to consider a pairwise attractive interaction (feature 1c in section 1.1) between particles which permits the spatial localisation of the flock. One could also consider the properties of the fluid where particles move. While this is not a problem for many systems (e.g. herds of mammals), it could be relevant in others, like schools of fishes or flock of birds. For example, if we have bacteria swimming in a fluid at very low Reynolds numbers, long-range hydrodynamics interaction are found to be dominant [20]. Another possibility is to change the last term of equations (1.1) to employ not metric interactions, but rather topological ones. This approach seems also to produce interesting results, since models employing such interactions predict flocks more cohesive than the metrical ones.

1.3 TOPOLOGICAL INTERACTIONS

In the vast majority of flocking models, including the Vicsek one, interactions between particles are defined employing the metric distance. This is a rather natural choice: animals have several ways to actually evaluate distances and are usually quite good at. Metric interactions, however, may not be suitable to reproduce the typical density changes of animal aggregations, since they predict that flock cohesion is lost when mutual distances become too large.

The concept of topological range has been proposed to solve this problem [21]. In this case, each individual interacts with a fixed number of neighbours, regardless of their actual distance. The central difference between a metric interaction and a topological interaction arises when studying different systems with different particles density. Indeed, if we change the density, the metric interaction strength varies, while the topological one stays constant. Therefore, topological interaction seems more suitable to describe cohesion of sparse flocks and when strong density fluctuations occurs.

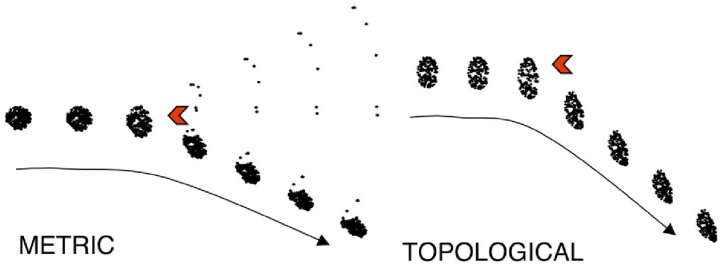

(a) Metric Interaction **(b)** Topological Interaction

Figure 1.2: Confrontation between metric and topological interaction under predator's attack. Black dots represent birds composing a flock, while the red arrow is a predator. Note that in (a) the flock scatters after the predator attack, while in (b) it remains cohese. Taken from [21].

To support this hypothesis, topological and metric have been confronted in the context of the Vicsek model (see section 1.2). In the classic Vicsek model every particle assumes the average direction of motion of the particles within a disk centred in itself, therefore such model is strictly metric. In a topological version of Vicsek model, instead, particles assume the mean direction of its n_C nearest neighbours, regardless of their actual metric distance. Without external perturbation, both interactions produce a single flock in an appropriate range of parameters. However, if we expose our system to a perturbation, namely a predator the outcome may change. Numerical simulations show that in systems subjected to metric interactions, flocks tend to break, while in systems with topological interactions flocks are more cohesive (see fig. 1.2).

Thanks to empirical studies on the spatial distribution of starling flocks[21], an estimate of the topological interaction has been proposed. Focusing on a single tagged bird, evidence shows that birds are isotropically distributed only over long distances, while locally birds seem to exhibit specific correlation in their dynamic. Such information can be used to evaluate the value of n_c, in this particular case it is found that $n_c \sim 7$. It is clear that the number of visually unobstructed neighbours around each bird is significantly higher than the topological interaction range found. Such inconsistency can be attributed to a probably insufficient object-tracking ability of the birds.

1.4 Hybrid Projection Model

Basic topological models, as the one presented in the previous section, predict the formation of cohese flocks, but they can not explain the great variety of flock dynamics observed in nature. It is therefore necessary to add supplementary features in the equations describing dynamics. Recently has been proposed the so called *Hybrid-Projection Model* [22] which employs topological interaction and presents all the features we presented in

section section 1.1.

Particles move in a plane with constant speed v_0. Their dynamics has two main features: an aligning and an attractive mechanism. Aligning mechanism (feature 2a) is implemented as in Vicsek model, but in a topological fashion, at every time-steps particles tend to take the average direction of their n_c nearest neighbours. We will indicate this component with $\langle\vec{\theta}_i\rangle_{\text{n.n}}$. The attraction mechanism, instead, is peculiar and it is actually the founding idea of the hybrid projection model. In a 2 dimensional space, an individual can not distinguish others if they are overlapped in its field of vision. The basic visual input to each individual can be assumed to be based simply on visual contrast: dark regions, corresponding to angular sectors where one or more particles block the line of sight of a tagged individual, and light regions (see fig. 1.3), corresponding to angular sectors where line of sight is not blocked by any other particle. The hybrid projection model use this visual input as a mean to introduce an attracting potential (feature 2b). Indeed, individuals are equally attracted to each of the dark domains, favouring motion towards high density zone of the space. This feature is modelised introducing the mean velocity direction:

$$\vec{\delta}_i = \frac{1}{N_i}\sum_{j=1}^{N_i}\begin{pmatrix}\cos(\theta_i^{(j)})\\ \sin(\theta_i^{(j)})\end{pmatrix} \quad , \tag{1.5}$$

where $\theta_i^{(j)}$ are the angles delimiting dark regions. Time evolution can be therefore written as:

$$\begin{cases} \vec{r}_i(t+\Delta t) &= \vec{r}_i(t) + \vec{v}_i(t)\Delta t \\ \vec{v}_i(t+\Delta t) &= v_0\phi_d\vec{\delta}_i + v_0\phi_a\langle\vec{\theta}_i(t)\rangle_{\text{n.n}} + \phi_n\eta_i(t) \end{cases} \quad , \tag{1.6}$$

where $\eta_i(t)$ is a noise term and ϕ_a, ϕ_d, ϕ_n are real positive weights such that $\phi_a + \phi_d + \phi_n = 1$ and which can be opportunely tuned. The presence of the projection term $\vec{\delta}$ provides a global interaction and, therefore, leads to rapid dynamic response, consistent with the fast transients observed in real flocks. This model is also robust in response to shocks, such as those caused by predation in real animal systems. Furthermore, in the original work [22], individuals are considered to have a non-zero volume (feature 1a) and provided with a blind range (feature 1d).

Tuning the free parameters of the model (ϕ_a, ϕ_d, ϕ_n, blind range size, shape and dimension of each individual) we can find several dynamical patterns, called *phenotypes*, which can also be observed in nature. They can be classified using the velocity magnetisation m, already defined in (1.3), and its typical trajectory of motion.

(a) Flocks with low magnetisation m values and weakly correlated internal dynamics, similar to the motion of a swarm of insects.

(b) Circulating flocks, similar to the motion sometimes observed in schools of fish.

(c) Flocks with high magnetisation m values, similar to the motion of travelling flocks of birds.

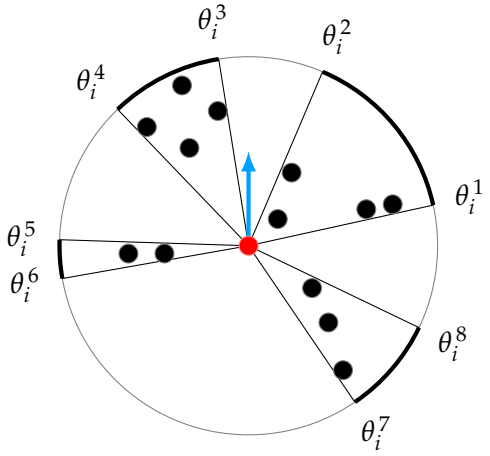

Figure 1.3: Diagram showing the construction of the projection in a 2-dimensional swarm, seen by the i-th individual.

1.5 Continuous Time version of the Vicsek model

Flocking models employing a topological interaction can give rise to a variety of realistic phenomenology. However they are mostly numerical models, since topological interactions are not easy to study via analytical means. Henceforth, if we do not want to rely only on numerical simulations we have to take a step back and reconsider metric interactions.

In this work, we introduce a continuous time version of the Vicsek model, which permits us to use standard analytical means, e.g. Fokker-Planck equations, to better inquire the model. There are, however, several ways to take the continuous limits of equations (1.1). Particularly equation (1.1c) is recasted into the form:

$$\dot{\theta}_i = -\tau \partial_{\theta_i} U\left(\theta_1, \vec{x}_i; \ldots; \theta_N, \vec{x}_N\right) + \sigma A_i(t) \ , \tag{1.7}$$

where τ is a constant, $U\left(\theta_1, \vec{x}_i; \ldots; \theta_N, \vec{x}_N\right)$ is an interaction potential favouring alignment and finally $A_i(t)$ is a gaussian random variable with momenta:

$$\langle A_i(t) \rangle = 0 \qquad \langle A_i(t) A_j(t') \rangle = \delta_{ij} \delta(t - t') \ . \tag{1.8}$$

This procedure leads to a set of Langevin equations describing an Ornstein-Uhlenbecch process on the velocity direction [23]. However, experimental data on the fish motion [24] show that such equations does not lead to a realistic model. More promising results are, instead, obtained employing a parameter ω describing the curvature of the particles trajectory [25], namely the first temporal derivative of velocity direction ($\omega \equiv \dot{\theta}$). Note that by using an Ornstein-Uhlenbech process on the curvature of the paricles, rather than their velocity direction, we are assuming that particles can not sustain too strongly curved trajectory.

After this brief introduction, we can finally introduce our model. This model describes the dynamics of N self-propelled particles, moving in a plane with constant speed v_0 and mutually interacting with potential U which favours their alignment (feature 4, section section 1.1). We, however, expect that every particle is subjected to a large, non predictable, number of random independent forces exerted by the environment. Furthermore, particle itself, thanks to its active properties, can oppose the environmental forces. This difficult situation is described by adding a stochastic noise term to the equations of the dynamics. This noise term, in virtue of the central limit theorem, can be regarded as gaussian.

The generalised coordinates of the i-th particle (with $i = 1 \dots N$) can be identified with its position $\vec{r}_i = (x_i, y_i)^t$, the velocity direction θ_i and the trajectory curvature ω_i of its motion. Langevin equations describing the dynamic of CTVM are written as follows:

$$\begin{cases} \dot{x}_i = v_0 \cos\theta_i & \text{(1.9a)} \\ \dot{y}_i = v_0 \sin\theta_i & \text{(1.9b)} \\ \dot{\theta}_i = \omega_i & \text{(1.9c)} \\ \dot{\omega}_i = -\gamma\omega_i - \partial_{\theta_i} U\left(\{\vec{r}_i, \theta_i\}_{i=1\dots N}\right) + \sigma A_i(t) & \text{(1.9d)} \end{cases} ,$$

where γ is an angular friction coefficient, $A_i(t)$ is a gaussian random variable with momenta:

$$\langle A_i(t) \rangle = 0 \qquad \langle A_i(t) A_j(t') \rangle = \delta_{ij}\delta(t - t') \tag{1.10}$$

for each $t, t' \in \mathbb{R}$, σ is a constant quantifying the system noise. Stochastic noise it is usually parameterised as $\sigma = \sqrt{2\gamma T}$, in order to favour the comparison with mesoscopic passive systems, where fluctuation-dissipation theorem stand. Note that temperature T has not actual physical meaning here, but it just quantifies noise. Such equations can be also written in a finite difference form, especially useful for numerical analyses purpose:

$$\begin{cases} x_i(t+\Delta t) &= x_i(t) + v_0 \cos(\theta_i(t))\Delta t \\ y_i(t+\Delta t) &= y_i(t) + v_0 \sin(\theta_i(t))\Delta t \\ \theta_i(t+\Delta t) &= \theta_i(t) + \omega_i(t)\Delta t \\ \omega_i(t+\Delta t) &= \omega_i(t) - \gamma\omega_i(t)\Delta t - \partial_{\theta_i} U \Delta t + \sqrt{2\gamma T}\Delta W_i(t)\sqrt{\Delta t} \end{cases} , \tag{1.11}$$

where $\Delta W_i(t)$ is a normally distributed random variable with null mean and unitary variance.

In order to modelise the tendency of biological units to assume the same direction as their neighbours, interacting potential U is chosen to be minimum when each particle is aligned with the other nearby ones. If particles are non point-like, interacting potential U must also include a repulsive (feature 1a) component. However we start our study examining point-like particles. In this case we can choose an interaction potential analogue to the ones used in ferromagnetic models:

$$U\left(\{\vec{r}_i, \theta_i\}_{i=1\dots N}\right) = \frac{1}{2}\sum_{i,j=1}^{N} \left[1 - \cos(\theta_i - \theta_j)\right] \mathrm{H}\left(R_{\text{int}} - \left\|\vec{r}_i - \vec{r}_j\right\|\right) , \tag{1.12}$$

where R_{int} is the interaction range of each particle and H is the Heaviside step function. Hence, for point-like particles, equations (1.9) are recast into:

$$\begin{cases} \dot{x}_i = v_0 \cos\theta_i & \text{(1.13a)} \\ \dot{y}_i = v_0 \sin\theta_i & \text{(1.13b)} \\ \dot{\theta}_i = \omega_i & \text{(1.13c)} \\ \dot{\omega}_i = -\gamma\omega_i - \sum_{j=1}^{N} \sin(\theta_i - \theta_j)\mathrm{H}\left(R_{\text{int}} - \left\|\vec{r}_i - \vec{r}_j\right\|\right) + \sqrt{2\gamma T}A_i(t) & \text{(1.13d)} \end{cases} .$$

Taking the over-damped limit of $\gamma \gg 1$, i.e. in hostile environments, in the last equation in (1.11), we easily find that our model maps into another continuous time version of the Vicsek model [23]:

$$\begin{cases} x_i(t+\Delta t) &= x_i(t) + v_0\cos(\theta_i(t))\Delta t \\ y_i(t+\Delta t) &= y_i(t) + v_0\sin(\theta_i(t))\Delta t \\ \theta_i(t+\Delta t) &= \theta_i(t) - \frac{1}{\gamma}\sin(\theta_i - \theta_j)\mathrm{H}\left(R_{\text{int}} - \left\|\vec{r}_i - \vec{r}_j\right\|\right)\Delta t + \sqrt{\frac{2\gamma T}{\gamma}}\Delta W_i(t)\sqrt{\Delta t} \end{cases} . \tag{1.14}$$

Furthermore, if we also employ the ferromagnetic potential (1.12) in the limit of $\theta_i - \theta_j \sim 0$ for each $i, j = 1 \dots N$, we easily obtain that last equation of (1.14) is recast into:

$$\theta_i(t+\Delta t) = \theta_i(t) - \frac{1}{\gamma}\sum_{j=1}^{N}(\theta_i - \theta_j) + \sqrt{\frac{2T}{\gamma}}\Delta W_i(t)\sqrt{\Delta t} \ . \tag{1.15}$$

While this expression is analogue to time evolution of Vicsek model (1.1), it still presents a feature that was absent in it. Indeed, in this model interaction lacks the normalisation factor $\frac{1}{N_R}$ and, therefore, the more is the number of particles in the neighbourhood of a given one, the stronger is the tendency of such unit to follow its neighbours.

Finally we remark that our model can not be studied in the contest of Hamiltonian formalism. Indeed equations (1.13) depends on the third derivative of position. This implies that no trivial conservation laws can be found, such as energy or total momentum.

1.5.1 Order Parameters

We now define some order parameters employed in this work in order to monitor the particles collective behaviour. First we will define the so called *velocity magnetisation* m, which monitors the degree of alignment of a system and therefore is useful to know if a flocking behaviour has arisen. Later we define the *spatial entropy* λ, in order to check if system shows spatial coherence, i.e. if particles have formed a group. Lastly, sometimes it is useful to know the size of a specific cluster and henceforth we will introduce the parameter σ_{cl}.

Velocity Magnetisation.
In order to follow the motion coherence, we define in analogy with ferromagnetic models, the *velocity magnetisation* m, already introduced in (1.3). Parameter m describes the degree of alignment of the particles:

$$m = \frac{1}{N} \left\| \sum_{j=1}^{N} \begin{pmatrix} \cos\theta_i \\ \sin\theta_i \end{pmatrix} \right\| \ . \tag{1.16}$$

With $m = 0$ we have that the system is in a totally disorganised state, while with $m = 1$ particles move all along in the same direction. Note that m is a function of the total momentum of the particles in the system, which in a classical mechanics system would be conserved. However, the model described by equations (1.9) has no Hamiltonian structure and thus conservation laws are lost. As a consequence, dynamic has no trivial constant of motion such as energy or total momentum.

Spatial Entropy.
Velocity magnetisation is not sufficient to describe the whole dynamics. Indeed we need to introduce a parameter measuring spatial coherence of the system. There are several possible choice, we choose to define a *spatial entropy* λ' in analogy with Shannon entropy. We divide the plane in W equal area cells, if $p_i(t)$ is the probability of finding a single particle in the i-th cell at a time t, then $\lambda'(t)$ is naturally defined as:

$$\lambda'(t) = -\sum_{i=1}^{W} p_i(t) \ln(p_i(t)) \ . \tag{1.17}$$

It is however more useful to employ a parameter λ which lives in the interval $[0, 1]$:

$$\lambda(t) = 1 - \frac{\lambda'(t)}{\ln W} \ . \tag{1.18}$$

With $\lambda = 0$ particles are equally distributed in each cell and thus we have no cluster formation; with $\lambda = 1$ particles are gathered in a single cell and have formed a single cluster.

Cluster Size.
Sometimes parameter λ is not sufficient to fully characterise spatial dynamics. For example, it do not give useful information on the size of the single clusters which may form in the system. Henceforth, we define the order parameter σ_{cl} which suggests the dimension of a certain particles cluster. It is easy to prove that, if we consider a uniform distribution over a set of circular shape with radius r, than its variance σ^2 respect the equation $\sigma^2 = \frac{1}{2}r^2$. Particles are assigned to a certain cluster watching their relative distance ftom Therefore, introducing the mean position of the cluster $\langle \vec{x} \rangle$ as:

$$\langle \vec{x} \rangle = \frac{1}{N_{\text{cl}}} \sum_{i \in \text{cluster}} \vec{x}_i \ , \tag{1.19}$$

where N_{cl} is the number of particles in a cluster, the parameter

(1.20)

is a good estimate of the cluster size. Note that, while order parameters m and λ refers to global properties of the system, cluster size σ_{cl} is defined locally, since there could be simultaneously several clusters with different dimension or even no clusters at all.

1.6 THE HAMILTONIAN MEAN FIELD MODEL

We start the study of our model, with a particular and simple case: particles moving in an unbounded domain and with an infinite interaction range R_{int}. While simple, this situation can be especially useful to implement an analytical approach to study the more general case.

With infinite interaction range, the set of equations (1.13d) and (1.13c) becomes independent of the spatial dynamics. Henceforth, if we are only interested in the angular dynamics, we can neglect spatial coordinates:

$$\begin{cases} \dot{\theta}_i &= \omega_i \\ \dot{\omega}_i &= -\gamma\omega_i - \partial_{\theta_i} U'_{\text{HMF}} + \sigma A_i(t) \end{cases} , \tag{1.21}$$

where:

$$U'_{\text{HMF}} = \frac{1}{2}\sum_{i,j=1}^{N}\left[1-\cos\theta_i-\theta_j\right] \quad . \tag{1.22}$$

Note that, while CTVM is not generally an Hamiltonian system, equations (1.21) describe the approach to equilibrium of a classical mechanics system with Hamiltonian:

$$H = \sum_{i=1}^{N}\frac{1}{2}\omega_i^2 + \frac{1}{2}\sum_{i,j=1}^{N}\left[1-\cos(\theta_i-\theta_j)\right]$$

or in a more generalised form:

$$H = \sum_{i=1}^{N}\frac{1}{2}\omega_i^2 + \frac{K}{2}\sum_{i,j=1}^{N}\left[1-\cos(\theta_i-\theta_j)\right] = \mathcal{T} + KU'_{\text{HMF}} \ , \tag{1.23}$$

where K is an arbitrary constant and $\mathcal{T}$ is the kinetic energy $\mathcal{T} = \frac{1}{2}\sum_{j=1}^{N}\omega_j^2$. A problem arises in the fact that this Hamiltonian does not guarantee thermodynamical stability [26]. Indeed, while kinetic energy $\mathcal{T}$ is of order $O(N)$, the potential energy U'_{HMF} scales as $O(N^2)$, hence the whole internal energy $H = \mathcal{T} + KU'_{\text{HMF}}$ scales as $O(N^2)$. Entropy S is an extensive quantity, therefore, in such case, free energy per particle $\frac{1}{N}F = \frac{1}{N}(H - TS)$ scales as $O(N)$ and therefore is infinite in the thermodynamical limit. There are several ways to fix the model, in this work we will use a potential energy $U_{\text{HMF}} = \frac{1}{N}U'_{\text{HMF}}$ so

that the whole internal energy H now scales as $O(N)$. Another way is to introduce an extensive tempe0rature $T' = TN$, so that TS now scale as $O(N^2)$ and is comparable with U. It is easy to prove that both ways will lead to equivalent physical results. The Hamiltonian now becomes:

$$H = \sum_{i=1} \frac{1}{2}\omega_i^2 + \frac{K}{2N} \sum_{i,j=1}^{N} \left[1 - \cos(\theta_i - \theta_j)\right] \quad . \tag{1.24}$$

A system described by such Hamiltonian is usually called Hamiltonian Mean Field model (HMF).

Equilibrium thermodynamic of this model can be exactly derived (see appendix A for more details). This system presents a second order transition in the magnetisation $m(T)$, with critical temperature $T_c = \frac{K}{2}$. The magnetisation $m(T)$ can be evaluated solving the implicit equation (see fig. 1.4a):

$$m(T) = \frac{I_1\left(\frac{Km}{T}\right)}{I_0\left(\frac{Km}{T}\right)} \ , \tag{1.25}$$

where I_1, I_0 are modified Bessel functions of the first kind. Energy per particle $e(T) = \frac{1}{N}H$, obeys the so called *heat equation* (see fig. 1.4b):

$$\frac{1}{2}\left(K(1 - m^2) + T\right) \quad . \tag{1.26}$$

Note that in fig. 1.4 we also compare data from numerical simulations (see appendix B for more details) with theoretical values. Computations display an almost perfectly compatibility between analytic and theoretical data. This results ensure us that the softwaress we will employ in later numerical simulations, work fine at least in this simple case.

1.6.1 From HMF to CTVM with finite interaction range

While HMF presents a nice analytic resolution, in our case it is not ideal since it describes the unrealistic situation where each particle interacts with all the others. However, HMF can be used to obtain an useful approximation of the CTVM dynamic in the spatially homogeneous case. This can be proven comparing the Fokker-Planck equations (FP) describing the dynamics of HMF (1.21) and CTVM(1.13), in the mean field approximation where the N particles distribution function can be factorised:

$$p_N(x_1, \ldots, x_N; t) = p_1(x_1, t) \cdots p_1(x_N, t) \ , \tag{1.27}$$

where x_1 stands for a set of variables needed to describe the system and p_1 is the single particle distribution function.

The FP describing HMF in the mean field approximation is derived in appendix C.1, it can be written as:

$$\partial_t p_1(\theta, \omega, t) = -\omega\partial_\theta p_1 + \partial_\omega(\gamma\omega p_1 + \partial_\omega p_1) + K\partial_\omega p_1 \phi^{\mathrm{HMF}}(\theta, t) \ , \tag{1.28}$$

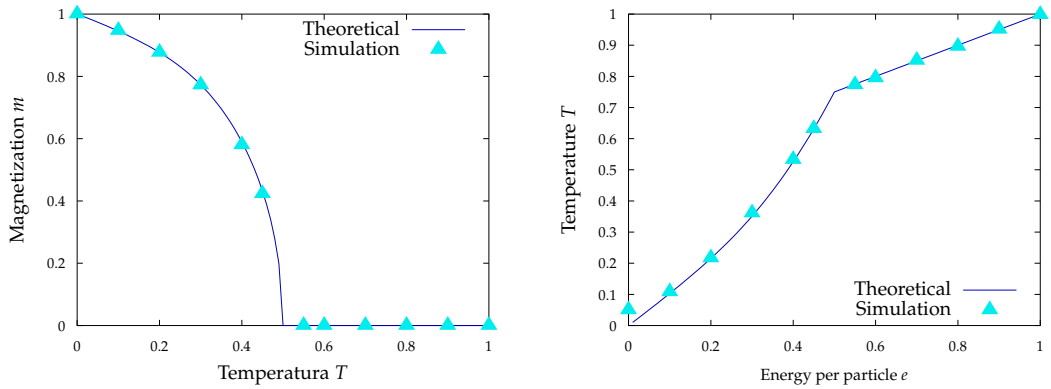

(a) Magnetisation as a function of temperature.

(b) Energy as a function of temperature.

Figure 1.4: Comparison between numerical simulation and theory in the HMF model. Simulations computed with $N = 200$, $\gamma = 1$ and $K = 1$.

where:

$$\phi^{\mathrm{HMF}}(\theta, t) = \int_{\mathbb{T}\times\mathbb{R}} \mathrm{d}\theta' \, \mathrm{d}\omega' p_1(\theta', \omega', t) \sin(\theta - \theta') \ . \tag{1.29}$$

CTVM dynamics is obviously more complicated since it involves also spatial variables. Its FP is computed in appendix C.2 and it is:

$$\partial_t p_1 = -v_0 \cos\theta \partial_x p_1 - v_0 \sin\theta \partial_y p_1 - \omega \partial_\theta p_1 + \partial_\omega \left(\gamma\omega + \mathfrak{D}\partial_\omega\right) p_1 + N\partial_\omega p_1 \Phi(\theta, t) \ , \tag{1.30}$$

where:

$$\Phi(\theta, t) = \int_{\mathbb{T}\times\mathbb{R}\times\mathbb{R}^2} \mathrm{d}\theta' \, \mathrm{d}\omega' \, \mathrm{d}\vec{x}' \ \sin(\theta - \theta') p_1(\theta', \omega', \vec{x}', t) \mathrm{H}\left(R_{\mathrm{int}} - \left\|\vec{x} - \vec{x}'\right\|\right) \ . \tag{1.31}$$

In order to compare (1.30) and (1.28), we focus on the angular dynamics, integrating equation (1.30) over the spatial variables. This operation results in:

$$\partial_t p_1 = -\omega \partial_\theta p_1 + \partial_\omega \left(\gamma\omega + \mathfrak{D}\partial_\omega\right) p_1 + N\partial_\omega p_1 \Phi(\theta, t) \tag{1.32}$$

If we consider that spatial and angular dynamics can be decoupled, we have that $p_1(\theta, \omega, \vec{x}, t) = p_1(\theta, \omega, t)\frac{\rho(\vec{x}, t)}{N}$, where ρ is the particles density. Furthermore, if we employ the approximation of a spatially homogeneous system, we have that $\rho(\vec{x}, t)$ is actually a constant. Using these considerations, equation eq. (1.31) is recast into:

$$\begin{aligned}\Phi(\theta, t) &= \frac{\rho}{N}\left(\int_{\mathbb{T}\times\mathbb{R}} \mathrm{d}\theta' \, \mathrm{d}\omega' \ \sin(\theta - \theta') p_1(\theta', \omega', t)\right)\left(\int_{\mathbb{R}^2} \mathrm{d}\vec{x}' \mathrm{H}\left(R_{\mathrm{int}} - \left\|\vec{x} - \vec{x}'\right\|\right)\right) \\ &= \frac{\rho}{N}\pi R_{\mathrm{int}}^2 \phi^{\mathrm{HMF}}(\theta, t)\end{aligned} \tag{1.33}$$

Therefore equation (1.32) is recast into:

$$\partial_t p_1 = -\omega \partial_\theta p_1 + \partial_\omega \left(\gamma\omega + \mathfrak{D}\partial_\omega\right) p_1 + N_R \phi^{\mathrm{HMF}}(\theta, t)\partial_\omega p_1 \ , \tag{1.34}$$

where N_R is $\rho\pi R_{\mathrm{int}}^2$. Note that the equation above is exactly (1.28) if $K \equiv N_R$.

We conclude that in the spatially homogeneous case, CTVM with finite R_{int} can be recast into the HMF, choosing as coupling constant K the mean number of particles inside the interaction range. Therefore, using equation (1.25), we have that magnetisation is well approximated by the implicit equation:

$$m(T) = \frac{I_1\left(\frac{N_R m}{T}\right)}{I_0\left(\frac{N_R m}{T}\right)} \ , \tag{1.35}$$

1.7 CTVM WITH PERIODIC BOUNDARY CONDITIONS

As a first step of the study of the CTVM, we consider a system with an indefinite number of particle moving in a limitless space. This is easily proven to be equivalent to a system with a finite number of particles, moving in a finite domain with periodic boundary conditions. This situation has been, already, extensively studied in a previous master thesis [27] and, therefore, we will just recall its main results using, however, original numerical simulations.

Periodic boundary conditions are not realistic and generally not suited to describe a system of biological units (e.g. birds). However, they are a basic construct commonly employed in complex systems because of their simplicity. They will also permit us to directly compare our model with the Vicsek original one.

Numerical simulations employ $N = 400$ particles moving in a square of side $L = 30$ with active speed $v_0 = 10$ and interaction range $R_{\mathrm{int}} = 3$. Generally, according to the dynamic of the velocity magnetisation m, the behaviour of the model seems to display a continuum phase transition at a certain critic temperature T_c, between a low temperature ordered phase and a high temperature disordered one. At low temperatures particles tend to quickly align and move towards the same direction. However, every direction is possible and the choice of a particular direction therefore represents a rotational symmetry breaking phenomenon. Indeed, dynamics is sometimes characterised by fast, synchronised change of angle of motion. Spatial dynamics, instead, seems to be dependent of the value of the friction coefficient γ. With low friction a small cluster, containing almost all particles, is quickly formed at low temperatures ($T < T_c$). With really high friction values, instead, cluster formation happens only in the absence of the noise term ($T = 0$), while at finite temperatures, particles move alongside a direction without an obvious spatial organisation.

We now shows the result of our simulations in two emblematic cases: a system with low angular friction ($\gamma = 1$) and a system with higher friction ($\gamma = 10$).

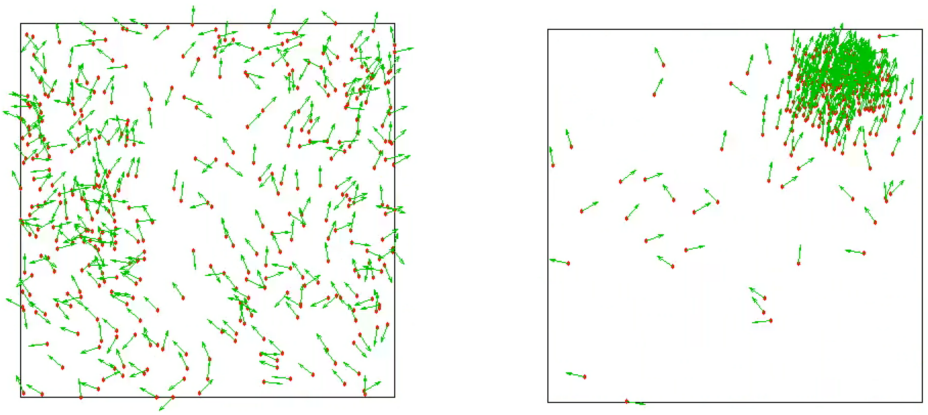

(a) $t \sim 10$.

(b) $t \sim 100$.

Figure 1.5: Snapshot of the system at two different times, showing the evolution from an initial disordered state, to an ordered state where almost all particles are gathered in a single cluster. Simulations computed with $N = 400$, $L = 30$, $R_{\text{int}} = 3$, $\gamma = 1$, $v_0 = 10$ and $T = 1$. Time-step used in computations $\Delta t = 0.01$.

Low Friction Regime

Characteristic of the low-friction regime is $\gamma = 1$. Simulations show that, with low noise ($T < 6.5$) particles tends to quickly align forming a small spatial cluster which moves altogether toward a direction(see fig. 1.5. With higher noise, particles neither form clusters, nor align. Results are depicted in fig. 1.6 and fig. 1.7. There seems to be two different phase transitions, one in the velocity magnetisation m and the other in the spatial entropy λ. The two transitions present two different critical temperature ($T \sim 6.5$ for m, $T \sim 5.5$ for λ).

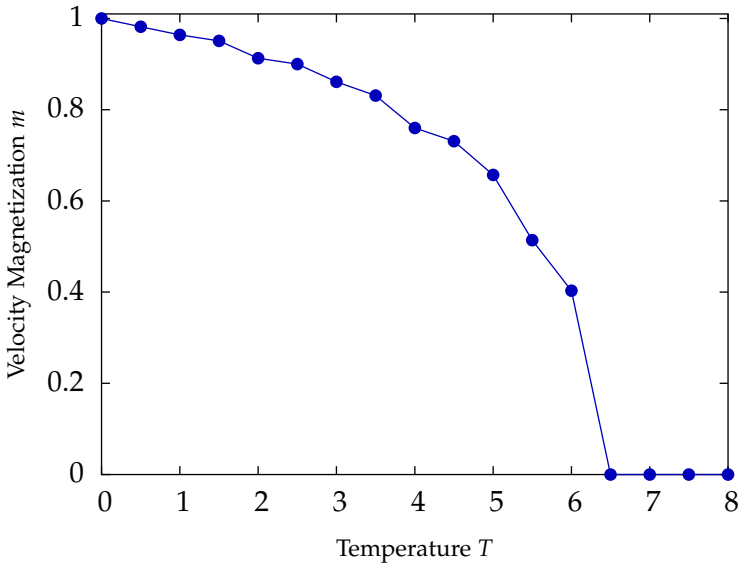

Figure 1.6: Magnetisation m as a function of the temperature. Simulations computed with $N = 400$, $L = 30$, $R_I = 3$, $\gamma = 1$, $v_0 = 10$. Time-step used in computations $\Delta t = 0.01$ for a total time of $t = 1000$.

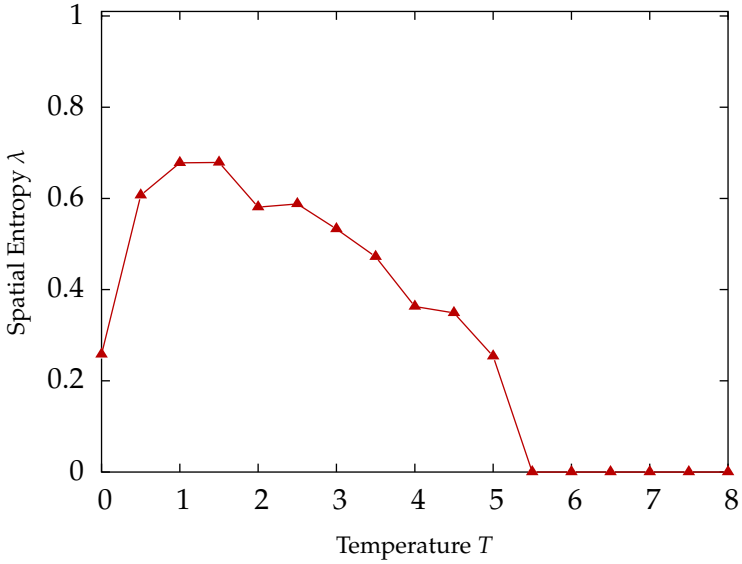

Figure 1.7: Spatial Entropy λ as a function of the temperature. Simulations computed with $N = 400$, $L = 30$, $R_I = 3$, $\gamma = 1$, $v_0 = 10$. Time-step used in computations $\Delta t = 0.01$ for a total time of $t = 1000$.

High Friction Regime

Characteristic of the high-friction regime is $\gamma = 10$. Regarding velocity magnetisation, as in the previous case, we can observe a continuum phase transition between an ordered phase and a disordered phase with critical temperature $T_c \sim 6.5$ (see fig. 1.8). However, spatial dynamics differs from the lower friction case. We can observe the creation of much bigger clusters than before, which are also not stable. Indeed, system sometimes collapse in a spatial desordered state and then, after a while, proceeds creating a new cluster. For the just mentioned reasons, parameter λ always present strong fluctuations in time dynamics, without ever, apparently, reaching a steady state. In this situation the system can be considered spatially homogeneous for most of the time, therefore we can compare numerical results with the mean field approximation described in section 1.6.1. As showed in fig. 1.8, the approximation seems almost perfect at low temperatures ($T < 4$), while at higher temperature data are underestimated by the mean field approximation. This probably due to diffusion effects which are more relevant the higher is temperature T.

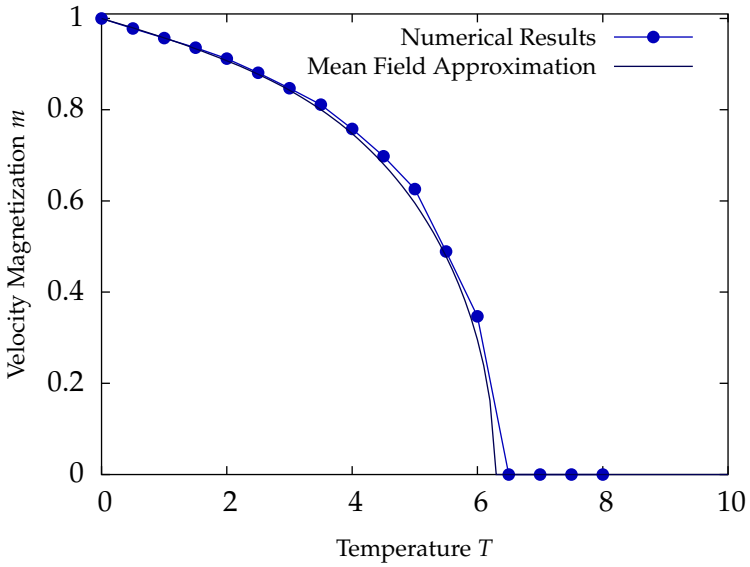

Figure 1.8: Magnetisation m as a function of the temperature. Simulations computed with $N = 400$, $L = 30$, $R_I = 3$, $\gamma = 1$, $v_0 = 10$. Time-step used in computations $\Delta t = 0.01$ for a total time of $t = 1000$.

CHAPTER 2

CTV MODEL WITH REFLECTING BOUNDARY CONDITIONS

A system of self-propelled particles with periodic boundary conditions is not realistic, since it assumes the existence of infinite particles. In fact if the system is actually composed of a finite number of individuals moving in space without boundaries and obeying equations (1.9), particles would most likely scatter in the space and clustering would not occur. To solve this problem one can introduce either an attractive interaction between particles (feature 1c, explained in section 1.1), or spatial constraints to the particles motion. In this chapter we will explore the second avenue by looking first at a system composed by N particles confined in a finite disk with reflecting boundary conditions.

Even if the idea to locate birds or fishes in a circular box seems weird, we can effectively use these boundaries to explain certain behaviour showed by bacteria in closed environments. Also, we could think of situations where all animals do not distance themselves from the same point for the time interval needed to form a flock.

Firstly, we will briefly discuss the existence of a collective rotating behaviour of particles in our system, employing an analytical approach. Later on, thanks to numerical simulations, we will show that, according to velocity magnetisation m, the system has a first-order transition between an ordered phase, characterised by a rotating behaviour, and a disordered phase. Such phase-transition is strictly correlated with the particles interaction range R_{int}. Indeed, we will prove that the ordered phase can not exists when the flock size becomes comparable with R_{int}, that is when all the particles in the flock are mutually interacting.

2.1 EXISTENCE OF A ROTATING BEHAVIOUR

In this section we will study, via analytical means, the behaviour of N point-like particles, moving in a disk with radius $\mathcal{R}_c$ and reflecting boundary conditions. Particularly, we will study equations (1.13) at sufficiently low temperatures to neglect the stochastic noise.

The presence of confining boundaries leads to the existence peculiar analytical solutions, where particles can actually gather and start rotating along the border of the confining circle. Our numerical simulations, which results are shown in later sections, show that such thing is actually the prevailing behaviour at low temperature in the ordered phase we observe.

A first, non trivial, problem we have to face is the analytical treatment of reflecting boundary conditions in a mechanical system. To achieve this result, we choose to study the N particles moving in a space with no boundaries, but in the presence of an external potential $\mathcal{U}_c(\vec{r}_1, \ldots, \vec{r}_N)$. This potential is defined to be dependent of an arbitrary parameter K such a way that, as $K \to \infty$, reflecting boundary conditions are recovered. There is no unique way to correctly define the effective confining potential $\mathcal{U}_c$, in this work we will use the form:

$$\mathcal{U}_c(\vec{r}_1, \ldots, \vec{r}_N) = \sum_{j=1}^{N} \frac{1}{2} K \left(\left\| \vec{r}_j \right\| - \mathcal{R}_c \right)^2 \mathrm{H} \left(\left\| \vec{r}_j \right\| - \mathcal{R}_c \right) \quad . \tag{2.1}$$

Equation (2.1) describes an half-harmonic potential acting outside the disk of radius $\mathcal{R}_c$. Henceforth, when a particle has a position $\vec{r}_i$ such that $\|\vec{r}_i\| < \mathcal{R}_c$, it is not subjected to any external force, while when $\|\vec{r}_i\| > \mathcal{R}_c$ an attractive force toward the inside of the disk is applied.

To employ potential (2.1) in the Langevin equations of our model. We observe that self-propelled particles move with constant speed. This constraint ($\left\|\dot{\vec{r}}\right\| = v_0$) is not holonomic [1] and, hence, would lead to not banal equations of motion. However, such a constraint is still ideal [28] and, therefore, we can proceed in analogy with classical mechanics to work out the effect of the external potential $\mathcal{U}_c$ onto the equations of motion. Namely, we impose a relation of the form

$$\ddot{\vec{r}}_i = v_0 \omega_i \begin{pmatrix} -\sin\theta_i \\ \cos\theta_i \end{pmatrix} - \partial_{\vec{r}_i} \mathcal{U}_c \quad , \tag{2.2}$$

by keeping constant the module of the velocity of each particle. Remembering that:

$$\ddot{\vec{r}}_i = \frac{\mathrm{d}}{\mathrm{d}t} \begin{pmatrix} v_0 \cos\theta \\ v_0 \sin\theta \end{pmatrix} = v_0 \dot{\theta}_i \begin{pmatrix} -\sin\theta_i \\ \cos\theta_i \end{pmatrix} \quad ,$$

we get an expression for the first derivative of θ_i:

$$\dot{\theta}_i = \omega_i + \frac{1}{v_0} \left(\sin\theta_i \partial_{x_i} - \cos\theta_i \partial_{y_i} \right) \mathcal{U}_c \quad . \tag{2.3}$$

[1] In classical mechanics a constraint is usually expressed as a function $f(q_1, \ldots, q_N, \dot{q}_1, \ldots, \dot{q}_N, t) = 0$. If function f does not depend on the time derivatives $\{\dot{q}_i\}_{i=1\ldots N}$ then the constraint is called *holonomic*, otherwise *non-holonomic*.

Hence, with potential (2.1), the equations of motion (1.13) can be recast into the form:

$$\begin{cases} \dot{x}_i = v_0 \cos\theta_i \\ \dot{y}_i = v_0 \sin\theta_i \\ \dot{\theta}_i = \omega_i + \frac{1}{v_0}\left(\sin\theta_i \partial_{x_i} - \cos\theta_i \partial_{y_i}\right) \mathcal{U}_c(\vec{r}_1, \ldots, \vec{r}_N) \\ \dot{\omega}_i = -\gamma\omega_i - \partial_{\theta_i} U + \sqrt{2\gamma T} A_i(t) \end{cases} . \tag{2.4}$$

By observing the obvious rotational symmetry of the system, it is natural to employ polar coordinates for the position vector $\vec{r}_i = (r_i \cos\phi_i, r_i \sin\phi_i)^t$. This gives:

$$\begin{aligned} \partial_{x_i}\mathcal{U}_c(\vec{r}_1, \ldots, \vec{r}_N) &= \cos\phi_i \partial_{r_i}\mathcal{U}_c(\vec{r}_1, \ldots, \vec{r}_N) \\ \partial_{y_i}\mathcal{U}_c(\vec{r}_1, \ldots, \vec{r}_N) &= \sin\phi_i \partial_{r_i}\mathcal{U}_c(\vec{r}_1, \ldots, \vec{r}_N) \end{aligned} .$$

Hence, equation (2.3) is recast into:

$$\begin{aligned} \dot{\theta}_i &= \omega_i + \frac{1}{v_0}\left(\sin\theta_i \cos\phi_i - \cos\theta_i \sin\phi_i\right) \partial_{r_i}\mathcal{U}_c(\vec{r}_1, \ldots, \vec{r}_N) \\ &= \omega_i + \frac{1}{v_0} \sin(\theta_i - \phi_i) \partial_{r_i}\mathcal{U}_c(\vec{r}_1, \ldots, \vec{r}_N) \end{aligned} \tag{2.5}$$

Doubts about the validity of this equation can be actually arisen, since, at $\omega_i = 0$, it has two fixed points:

- $\theta_i = \phi_i$: particle is moving radially outward the disk;
- $\theta_i = \phi_i + \pi$: particle is moving radially inward the disk.

However, by linearising equation (2.5) around these two points and taking into account that $\partial_{r_i}\mathcal{U}_c > 0$ when $r_i > \mathcal{R}_c$, we find that the first fixed point is unstable while the second one is stable whenever the particle is outside the confining disk.

The equations (2.4) in polar coordinates are then given by:

$$\begin{cases} \dot{r}_i &= v_0 \cos(\theta_i - \phi_i) \\ r_i\dot{\phi}_i &= v_0 \sin(\theta_i - \phi_i) \\ \dot{\theta}_i &= \omega_i + \frac{1}{v_0}\sin(\theta_i - \phi_i)\partial_{r_i}\mathcal{U}_c(\vec{r}_1, \ldots, \vec{r}_N) \\ \dot{\omega}_i &= -\gamma\omega_i - \partial_{\theta_i} U + \sqrt{2\gamma T} A_i(T) \end{cases} . \tag{2.6}$$

We are now ready to prove that, at $T \sim 0$, a solution of the dynamical system describes a rotating collective behaviour. Suppose that a point-like, perfectly oriented, cluster is formed. Such hypothesis, along with the absence of the noise term, implies that mutual interactions can be neglected. Therefore, it is possible to reduce the dynamical system to one describing of the motion of a single particle subjected to external potential (2.1).

$$\begin{cases} \dot{r} &= v_0 \cos(\theta - \phi) \\ r\dot{\phi} &= v_0 \sin(\theta - \phi) \\ \dot{\theta} &= \omega + \frac{K}{v_0}\sin(\theta - \phi)\,(r - \mathcal{R}_c)\,\mathrm{H}\,(r - \mathcal{R}_c) \\ \dot{\omega} &= -\gamma\omega \end{cases} . \tag{2.7}$$

	Theoretical	Numerical
$\dot{\phi}^\star$	0.639	0.637 ± 0.008
$r^\star$	15.6394	15.6 ± 0.2
$\omega^\star$	0	0.000 ± 0.001

(a) $K = 10$

	Theoretical	Numerical
$\dot{\phi}^\star$	0.66367	0.664 ± 0.004
$r^\star$	15.066373	15.07 ± 0.01
$\omega^\star$	0	0.000 ± 0.001

(b) $K = 100$

Table 2.1: Typical dynamical values of the steady state (2.8) compared with numerical simulations results. Numerical parameters are: $\gamma = 1$; $N = 400$; $\mathcal{R}_c = 15$; $R_{\text{int}} = 3$; $v_0 = 10$; $T = 0$.

In a rotating solution, if it exists, the particle cluster has a constant distance from the origin (i.e. $\dot{r} = 0$). It is easy to check that there exists two solutions respecting such conditions:4

$$\begin{cases} r^\star(t) & \equiv & \mathcal{R} \\ \phi^\star(t) & = & \pm\frac{v_0}{\mathcal{R}}t \\ \theta^\star(t) & = & \pm\frac{v_0}{\mathcal{R}}t \pm \frac{\pi}{2} \\ \omega^\star(t) & \equiv & 0 \end{cases} \tag{2.8}$$

where $\mathcal{R}$ is a solution to equation:

$$\frac{v_0^2}{\mathcal{R}} = K\left(\mathcal{R} - \mathcal{R}_c\right) \ , \tag{2.9}$$

that is $\mathcal{R} = \frac{1}{2}\left(\mathcal{R}_c + \sqrt{\mathcal{R}_c^2 + 4\frac{v_0^2}{K}}\right)$. Note that $R \to \mathcal{R}_c$, as $K \to \infty$.

We check if our numerical simulation software correctly predicts such results. We simulated a system of $N = 400$ particles, moving with equations (2.6) with finite K. Results (shown in table 2.1) are in good agreement with theoretical predictions.

Numerical simulations suggest that the steady state (2.8) is actually an attractor (see fig. 2.1) for a suitable number of starting conditions. Our analytical attempts to prove such a fact all failed. Indeed, a standard analytical approach to prove stability would be to linearize differential equations (2.5) around the steady state. However, the presence of an Heaviside theta function in potential (2.1) makes linearising possible only in the small interval $[r^\star - \frac{1}{K}, r^\star + \frac{1}{K}]$. Henceforth, in the limit of $K \to \infty$, system is not linearizable. Another possible analytical approach is to find a suitable Lyapunov function, but we could find none.

Numerical simulations, also, show that, while the rotating state is an attractor, it becomes unstable above a given time t_s. However, the stability time t_s seems to be a fast increasing function of K. It is, therefore, legit to think that as $K \to \infty$ we have t_s also goes to infinity.

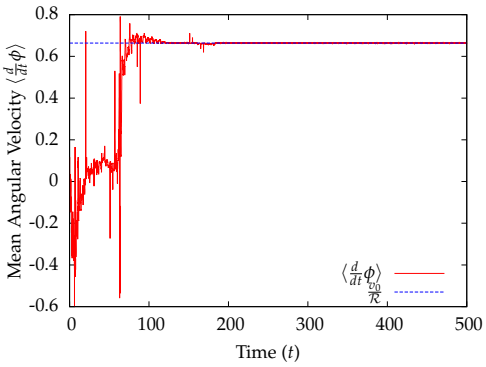

(a) Approach to the steady state of $\langle \frac{d}{dt}\phi(t) \rangle$.

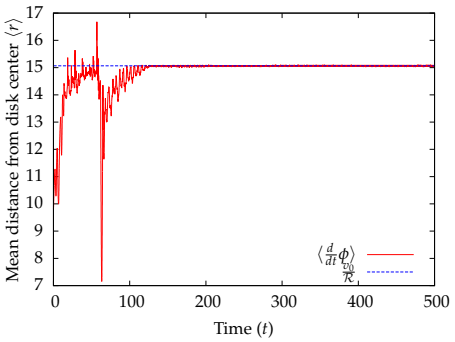

(b) Approach to the steady state of $\langle r(t) \rangle$.

Figure 2.1: $r_i(t)$, $\phi_i(t)$, approach to the steady state at $T = 0$ with $K = 100$. $\langle x(t) \rangle$ calculated as $\langle x(t) \rangle = \frac{1}{N} \sum_{i=1}^{N} x_i(t)$. Numerical parameters are: $\gamma = 1$; $N = 400$; $\mathcal{R}_c = 15$; $R_{\text{int}} = 3$; $v_0 = 10$; time-step $\Delta t = 0.01$; total elapsed time $t = 4000$.

2.2 Numerical Results

We now employ numerical methods, described in appendix B, to get a more detailed analysis of the dynamical behaviour of our system. As already said, we observe the existence of two different phases:

1. at low temperature all particles quickly gather, forming a small cluster which rotates alongside the border, we call this state *rotation phase*;
2. at higher temperature, instead, particles do not move coherently, we call this state *disordered phase*.

In the rotation phase, particles can rotate in two different directions: clockwise and counterclockwise. Henceforth, we can supposed that this phase arises as a $\mathbb{Z}_2$ symmetry breaking phenomenon. Note that this was foreseen by the existence of two distinct rotating steady states in (2.8)

When particle rotates, they also display two possible configurations, one less dense than the other (see fig. 2.2). There seems not to be a preferred configuration; numerical simulations show that they arise with the same frequency. Permanence time in each state, seems to be dependent on the amount of stochastic noise in the system. At really low temperature permanence times can be really long; at higher temperatures particles jump from a configuration to the other quite often. If we call $\sigma_{\text{cl}}^{(\text{s})}(T)$ the cluster size associated to the sparse configuration at temperature T and $\sigma_{\text{cl}}^{(\text{c})}(T)$ the same for the compact one, we find that $\sigma_{\text{cl}}^{(\text{s})} - \sigma_{\text{cl}}^{(\text{c})}$ is an increasing function of the temperature. Sparse configuration is also less ordered than the compact one and is therefore associated with a smaller value of velocity magnetisation m(see fig. 2.3).

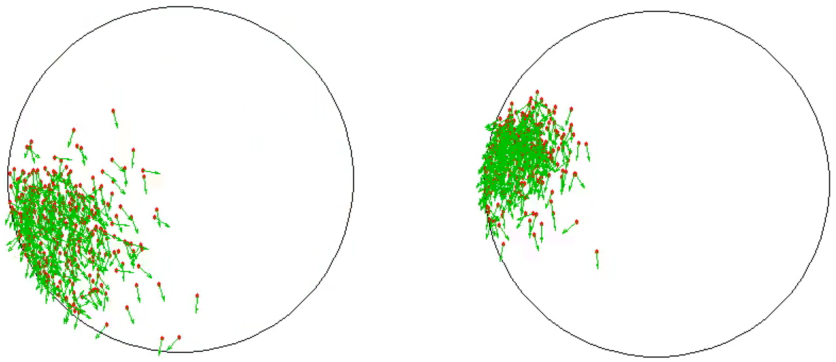

(a) Sparse configuration

(b) Compact configuration

Figure 2.2: Two snapshots of the same system at different times, showing the two possible state: (a) sparse; (b) compact. Numerical parameters are: $\gamma = 10$; $N = 400$; $\mathcal{R}_c = 15$; $R_{\text{int}} = 30$; $v_0 = 10$; time-step $\Delta t = 0.01$.

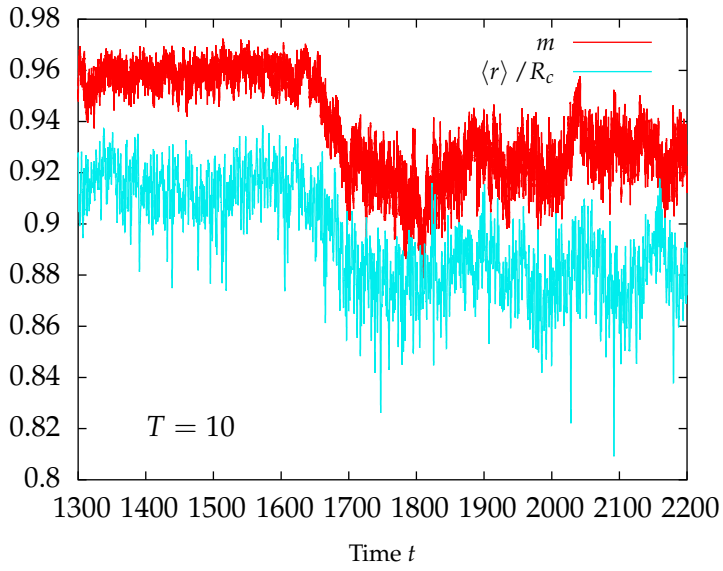

Figure 2.3: Particular of the time evolution of the velocity magnetisation m and mean radial distance of the particles $\langle r \rangle$, normalised over $\mathcal{R}_c$. This picture, show how at greater mean distance from the border, which is associated to a bigger cluster, corresponds a smaller value of m. Numerical parameters are: $T = 10$; $\gamma = 1$; $N = 400$; $\mathcal{R}_c = 15$; $R_{\text{int}} = 5$; $v_0 = 10$; time-step $\Delta t = 0.01$.

2.2.1 Comparison with Periodic Boundaries Conditions

To directly compare the result obtained in 1.7 with this case, we use the same numerical parameters as in the previous section, that is fixed the confining radius $\mathcal{R}_c$ to a value of $\mathcal{R}_c = 15$; the interaction range to $R_{\text{int}} = 3$; the number of particles to $N = 400$; and the particles speed to $v_0 = 10$.

The two boundaries lead to totally different outcomes. While with periodic boundaries conditions one observe a continuous phase transition, while with reflecting boundaries conditions a first order transition is detected. At each temperature where particles are in the rotation phase, velocity magnetisation is $m \sim 1$, that is particles are almost perfectly aligned. However, if we "heat" the system to the critical temperature T_c, we have an abrupt phase transition where particles go from a perfectly ordered phase with $m \sim 1$ to a seemingly disordered phase where $m \sim 0$.

Low Friction Coefficient

Characteristic of the low-friction regime is $\gamma = 1$.

Simulations show that, with low noise ($T < 6.5$) particles tends to quickly align forming a small cluster (see figs. 2.4 and 2.5) in space which rotates sticking to the boundary circle. With higher noise, particles neither form clusters, nor align.

Due to the low critical temperature shown by the system with the parameters employed ($6 \lesssim T_c \lesssim 7$), rotational phase exists only at relatively low temperatures. Unfortunately, this imply that it is really difficult to correctly identify the sparse and the compact configurations of the rotating particles, checking only parameters m and λ. However, presence of two rotating phase is easily shown studying parameter σ_{cl} (see fig. 2.6).

Note that phase transition occurs only when the cluster size σ_{cl} of the sparse configuration reaches $\sigma_{\text{cl}} \sim 1.5 = \frac{1}{2} R_{\text{int}}$. This suggests that interaction between particles, following potential 1.12, is actually weak, since to have stability of a cluster we have to ensure that every particles is interacting with each other, condition assured when $\sigma_{\text{cl}} < \frac{1}{2} R_{\text{int}}$.

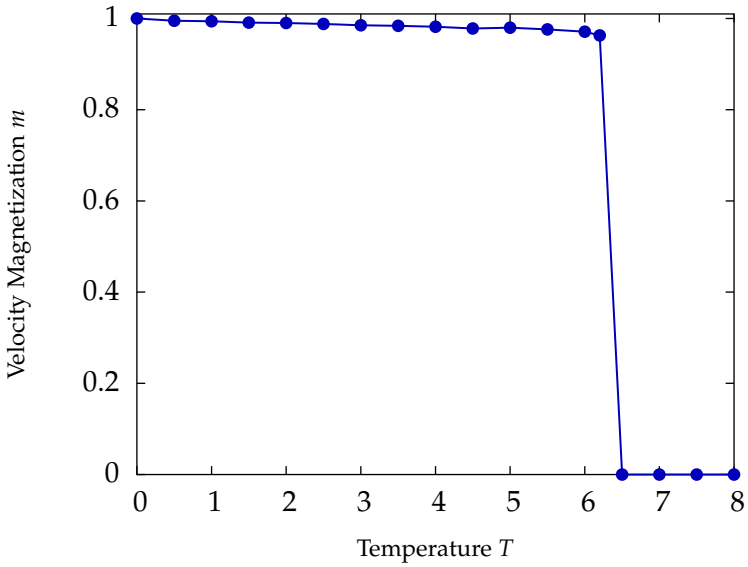

Figure 2.4: Reflecting-boundaries low-friction velocity magnetisation m transition. Data have been obtained as a time average after convergence to a stationary regime. Numerical parameters are: $\gamma = 1$; $N = 400$; $\mathcal{R}_c = 15$; $R_{\text{int}} = 3$; $v_0 = 10$; time-step $\Delta t = 0.01$; total elapsed time $t = 4000$.

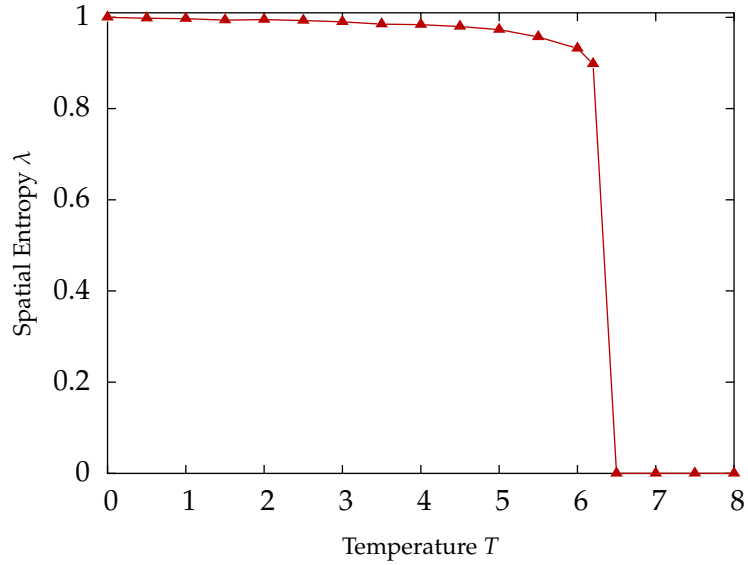

Figure 2.5: Reflecting-boundaries low-friction spatial entropy λ transition. Data have been obtained as a time average after convergence to a stationary regime. Numerical parameters are: $\gamma = 1$; $N = 400$; $\mathcal{R}_c = 15$; $R_{\text{int}} = 3$; $v_0 = 10$; time-step $\Delta t = 0.01$; total elapsed time $t = 4000$.

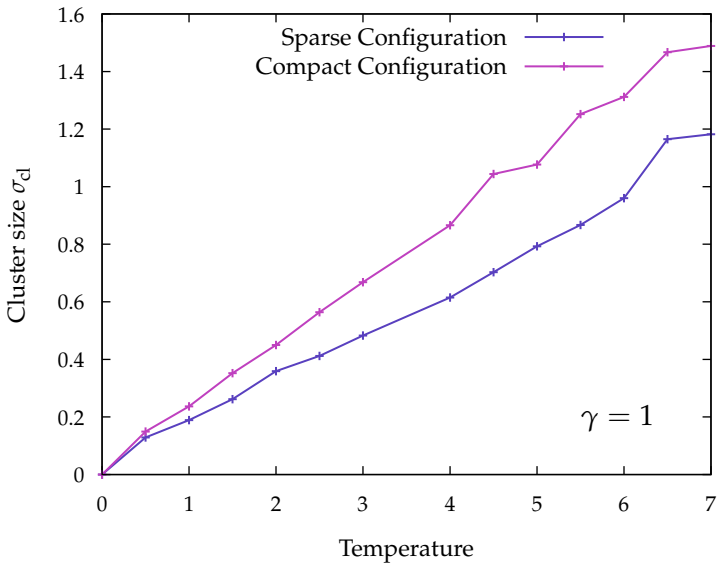

Figure 2.6: Cluster size $\sigma_c l$ as a function of temperature. Data obtained thanks to numerical simulations using parameters $N = 400$, $\mathcal{R}_c = 15$, $R_{\text{int}} = 3$, $v_0 = 10$; time-step $\Delta t = 0.01$; total elapsed time $t = 4000$.

High Friction Coefficient

With respect to the previous case, the friction coefficient is increased to $\gamma = 10$.

Results are similar to those of the low-friction regime (see figs. 2.7 to 2.9). At low temperature ($T \lesssim 1.5$), however, convergence time needed to form a unique spatially-localised cluster is much longer than in the low friction case (see fig. 2.10). In this case time evolution is characterised by the formation of several small clusters which rotate with different speed along the borders and which eventually join. Indeed, at $T = 0$ during we are not even able to observe the cluster formation as it probably takes extremely long times. This is the reason why in the values $m(0)$ and $\lambda(0)$ are not equal to one.

As in the low friction case, we have that the maximum value reached by the sparse phase (see fig. 2.9) is about $\frac{1}{2}R_{\text{int}}$.

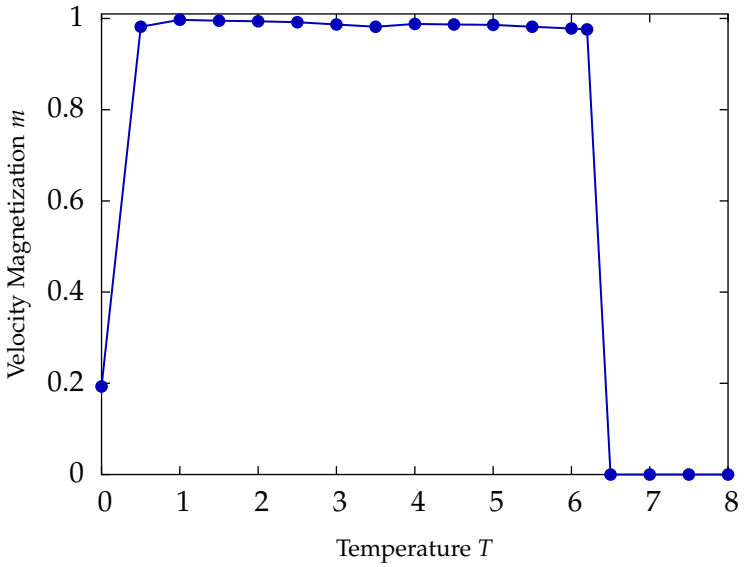

Figure 2.7: Reflecting-boundaries low-friction velocity magnetisation m transition. Data have been obtained as a time average after convergence to a stationary regime. Numerical parameters are: $\gamma = 10$; $N = 400$; $\mathcal{R}_c = 15$; $R_{\text{int}} = 3$; $v_0 = 10$; time-step $\Delta t = 0.01$; total elapsed time $t = 4000$.

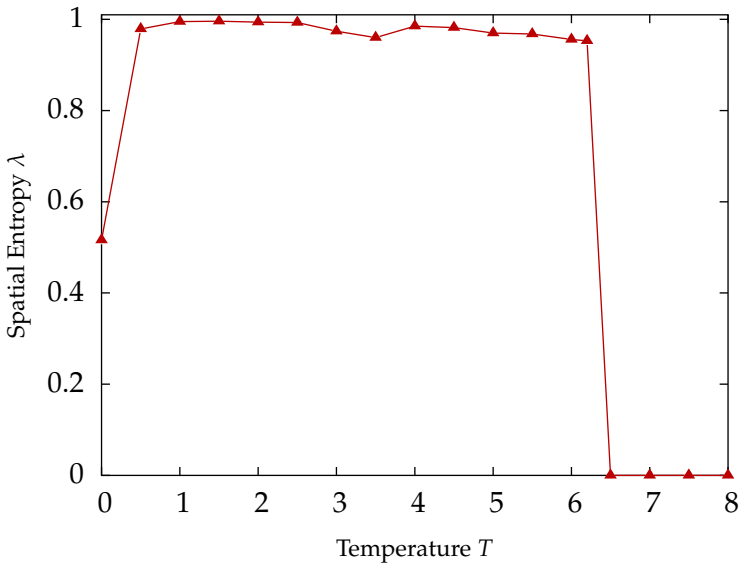

Figure 2.8: Reflecting-boundaries low-friction spatial entropy λ transition. Data have been obtained as a time average after convergence to a stationary regime. Numerical parameters are: $\gamma = 10$; $N = 400$; $\mathcal{R}_c = 15$; $R_{\text{int}} = 3$; $v_0 = 10$; time-step $\Delta t = 0.01$; total elapsed time $t = 4000$.

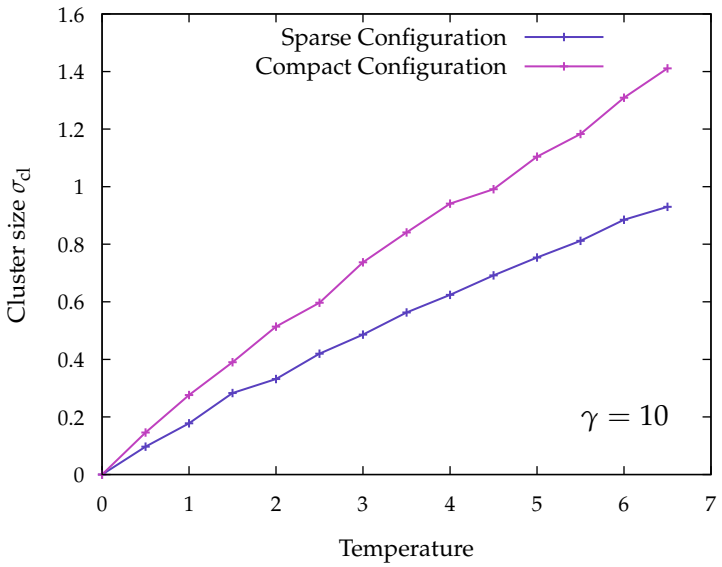

Figure 2.9: Cluster size $\sigma_c l$ as a function of temperature. Data obtained thanks to numerical simulations using parameters $N = 400$, $\mathcal{R}_c = 15$, $R_{\text{int}} = 3$, $v_0 = 10$; time-step $\Delta t = 0.01$; total elapsed time $t = 4000$.

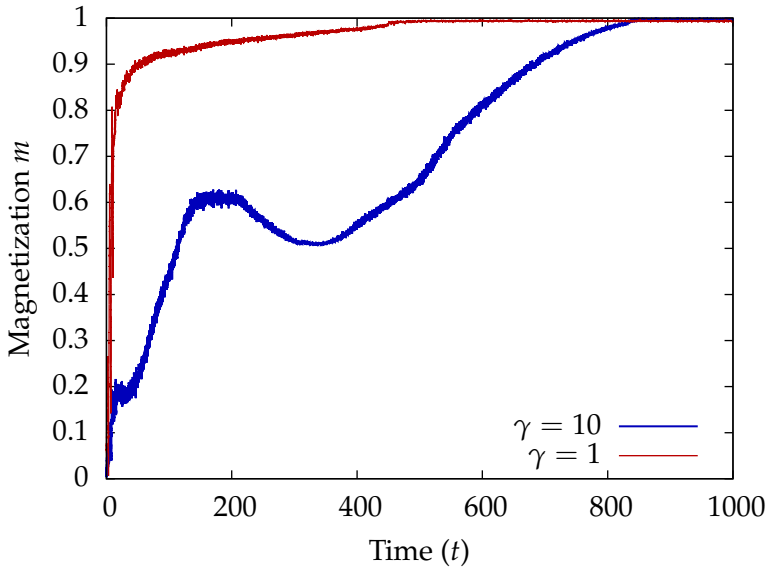

Figure 2.10: Comparison between the time evolution of the magnetisation m in the low friction case ($\gamma = 1$) and the high friction one ($\gamma = 10$). Note that the low friction system reach the steady phase much faster. Numerical parameters: $N = 400$; $T = 1$; $\mathcal{R}_c = 15$; $R_{\text{int}} = 3$; $v_0 = 10$.

Stability of the Rotating Phase

By looking at figs. 2.4 and 2.7, we can ask ourselves if what we are observing is a true phase transition. Indeed, one could object that for any fixed temperature, waiting a sufficient long time, an ordered phase and a rotating behaviour would arise.

To check the validity of this claim, we can study the stability of the rotating behaviour as a function of the temperature. The simpler method to achieve this, is to make some numerical simulations, setting as initial conditions the analytical steady state found in the previous section (eqs. (2.8)). If we find a temperature T_{st} above which the system always converges to a disordered state, then we have proven that rotating behaviour is not always stable and that a critical temperature indeed exists.

Numerical simulations outcomes are shown in table 2.2. As expected, we find a finite value for T_{st} that it is slightly greater of the corresponding critical temperature computed in the previous section. There are several possible explanations to this phenomenon. First, it is possible that the temperature T_{st} is not necessarily equal to the critical temperature T_c, but we surely have that $T_{\text{st}} \geq T_c$. Indeed, one does expect that the basin of attraction of the rotating behaviour size shrinks as temperature increases. Therefore,it could exists a temperature interval $T_c \leq T \leq T_{\text{st}}$ where the ordered phase is stable, but it is an attractor only for a really small number of starting conditions. Secondly, the observed difference between T_c and T_{st} could simply be a problem related to insufficent simulation times.

Friction Value	Stability Temperature	Critical Temperature
$\gamma = 1$	$7 \leq T_{\text{st}} \leq 7.5$	$6.2 \leq T_c \leq 6.5$
$\gamma = 10$	$6.5 \leq T_{\text{st}} \leq 7$	$6.2 \leq T_c \leq 6.5$

Table 2.2: Comparison between the stability temperature T_{st} and the critical temperature T_c. Data obtained thanks to numerical simulations using parameters $N = 400$, $\mathcal{R}_c = 15$, $R_{\text{int}} = 3$, $v_0 = 10$; time-step $\Delta t = 0.01$; total elapsed time $t = 4000$.

2.2.2 System Behaviour with Larger Range of Interaction

Numerical simulations show that, at fixed temperatures, a variation of the interaction range does not influence the values of m or λ. Thus, when we are dealing with low temperatures ($T < 7$) we expect to find the same results as in the previous section. Role of interaction range is, instead, crucial when examining the stability of the rotating state. Indeed the critical temperature T_c seems to be strongly dependent on interaction range: the higher R_{int} is, the higher T_c will be. Therefore, if we use a large value of R_{int} we can therefore study the properties of the rotating state at higher temperatures than before.

For small interaction range (as in section 2.2.1) magnetisation seems to be a constant function of the temperature. However, if we increase R_{int}, we can observe that this is false and that magnetisation is just a slow decreasing function of temperature. Therefore,

as we raise R_{int}, we observe an always less abrupt phase transition (see for example figs. 2.12 and 2.15).

As typical temperatures are higher than in the small R_{int} case, we can finally observe that the two possible rotating configurations (the sparse and the compact one) actually play an important role for the dynamics of the velocity magnetisation m. We remark that particles seems to jump from a configuration to an another randomly and none of the two seems to be preferred. The existence of two distinct phases is also suggested by the magnetisation m and entropy λ distributions during the rotation phase, where two clearly distinct peaks can be observed (see fig. 2.11).

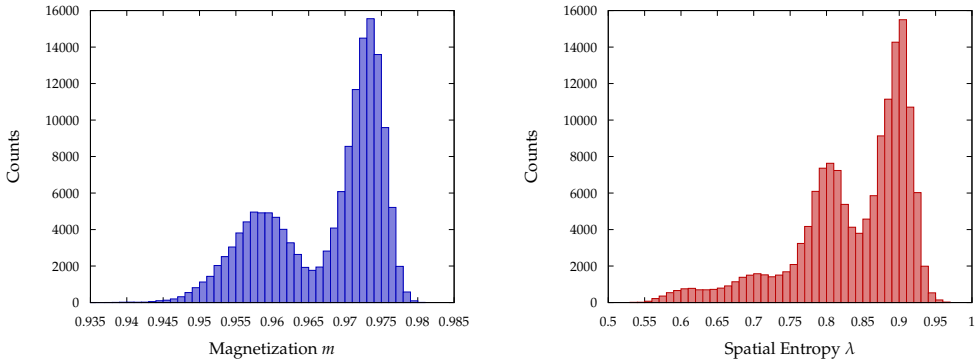

(a) Magnetisation m **(b)** Spatial entropy λ

Figure 2.11: Two histograms showing the coexistence of two separate phases. Numerical parameters are: $T = 9$; $\gamma = 10$; $N = 400$; $\mathcal{R}_c = 15$; $R_{\text{int}} = 5$; $v_0 = 10$; time-step $\Delta t = 0.01$.

We fix the confining radius $\mathcal{R}_c$ to a value of $\mathcal{R}_c = 15$; the interaction range to $R_{\text{int}} = 5$; the number of particles to $N = 400$; and the particles velocity to $v_0 = 10$. As usual, we will examine our system behaviour at low and high friction regimes.

Low Friction

We set the friction coefficient to $\gamma = 1$. Simulations show results similar to the one in section 2.2.1 and are shown in figs. 2.12 to 2.14. Indeed we find that a first order transition still occurs, but the critical temperature T_c is higher than before ($13 \lesssim T \lesssim 14$). Note that at $T \lesssim 7$ magnetisation and spatial entropy values are comparable with the ones found in the previous section. At higher temperatures ($T > 7$), instead, the two spatial configurations can be recognised also in the velocity magnetisation and spatial entropy diagrams. Indeed, the difference in the flock size in these two configuration increases with temperature.

As we already noted, phase transition occurs when cluster size in the sparse phase become comparable with $\frac{1}{2}R_{\text{int}}$.

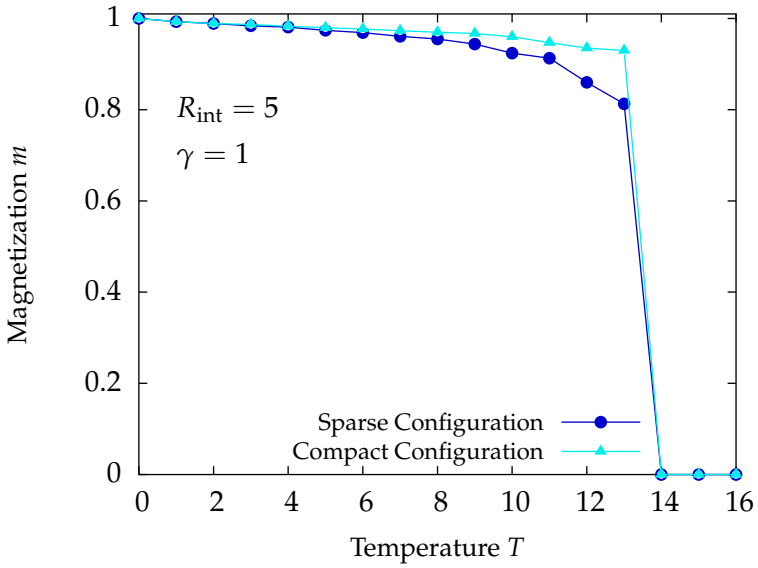

Figure 2.12: Reflecting-boundaries low-friction clustering transition. Data have been obtained as a time average after convergence to a stationary regime. Numerical parameters are: $\gamma = 1$; $N = 400$; $\mathcal{R}_c = 15$; $R_{\text{int}} = 5$; $v_0 = 10$; time-step $\Delta t = 0.01$; total elapsed time $t = 4000$.

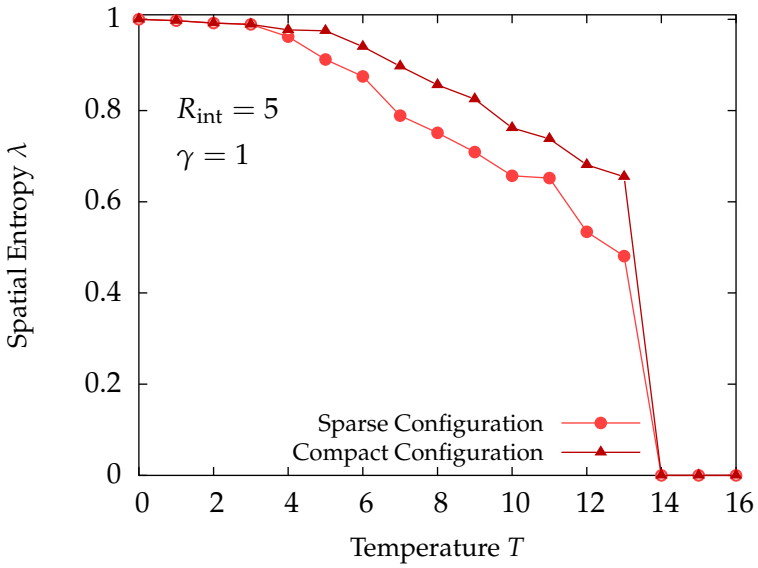

Figure 2.13: Reflecting-boundaries low-friction clustering transition. Data have been obtained as a time average after convergence to a stationary regime. Numerical parameters are: $\gamma = 1$; $N = 400$; $\mathcal{R}_c = 15$; $R_{\text{int}} = 5$; $v_0 = 10$; time-step $\Delta t = 0.01$; total elapsed time $t = 4000$.

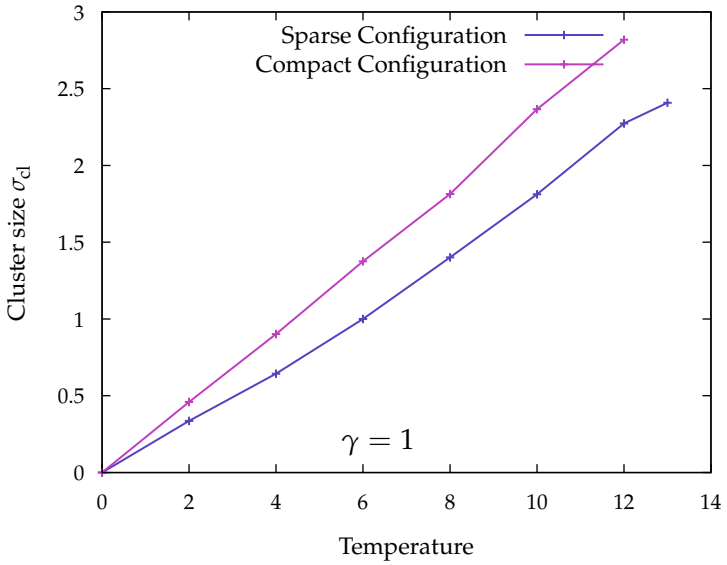

Figure 2.14: Cluster size $\sigma_c l$ as a function of temperature. Data obtained thanks to numerical simulations using parameters $N = 400$, $\mathcal{R}_c = 15$, $R_{\text{int}} = 3$, $v_0 = 10$, $\gamma = 1$; time-step $\Delta t = 0.01$; total elapsed time $t = 4000$.

High Friction

Friction coefficient is increased to $\gamma = 10$. The behaviour of the system is really similar to the low friction case; results are shown in fig. 2.15 and fig. 2.16. However, note that, at a fixed temperature of the rotating phase, magnetisation and entropy are generally higher than in the previous case. This is associated with the onset of the clusters where dimension is larger than the ones observed in the low friction case. Furthermore, the cluster size at high temperatures, suggests that σ_{cl} is not a perfect linear function of temperature T.

We also remark that, as in section 2.2.1, with $T = 0$ and $\gamma = 10$, the system seems to never reach the expected phase with $m \sim 1$ and $\lambda \sim 1$; this is probably due to the existence of several metastable states, which at $T > 0$ cease to exist.

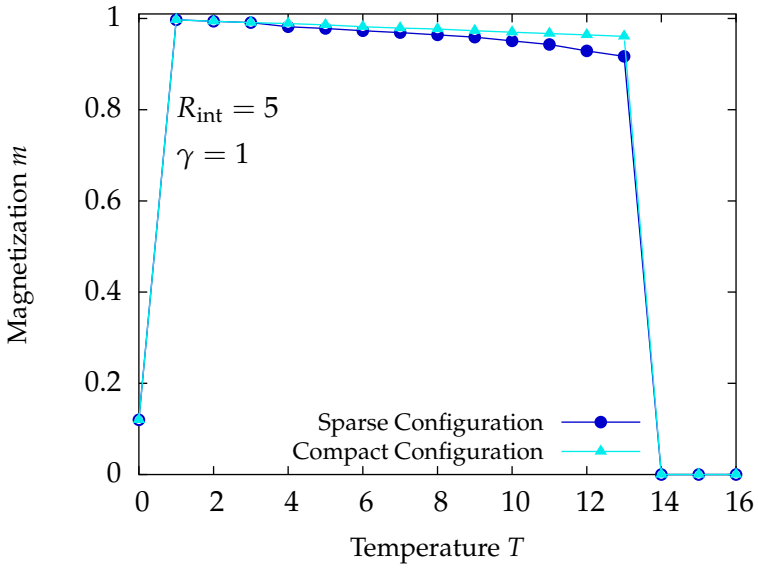

Figure 2.15: Reflecting-boundaries low-friction clustering transition. Data have been obtained as a time average after convergence to a stationary regime. Numerical parameters are: $\gamma = 10$; $N = 400$; $\mathcal{R}_c = 15$; $R_{\text{int}} = 5$; $v_0 = 10$; time-step $\Delta t = 0.01$; total elapsed time $t = 4000$.

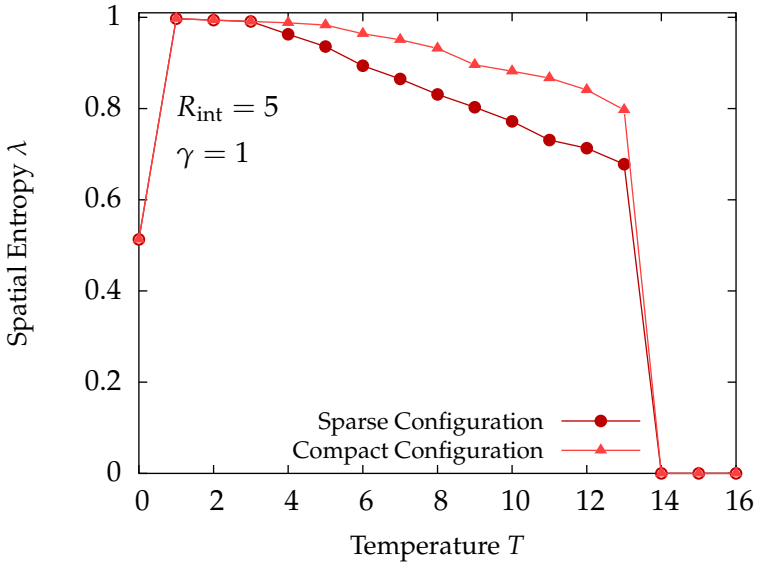

Figure 2.16: Reflecting-boundaries low-friction clustering transition. Data have been obtained as a time average after convergence to a stationary regime. Numerical parameters are: $\gamma = 10$; $N = 400$; $\mathcal{R}_c = 15$; $R_{\text{int}} = 5$; $v_0 = 10$; time-step $\Delta t = 0.01$; total elapsed time $t = 4000$.

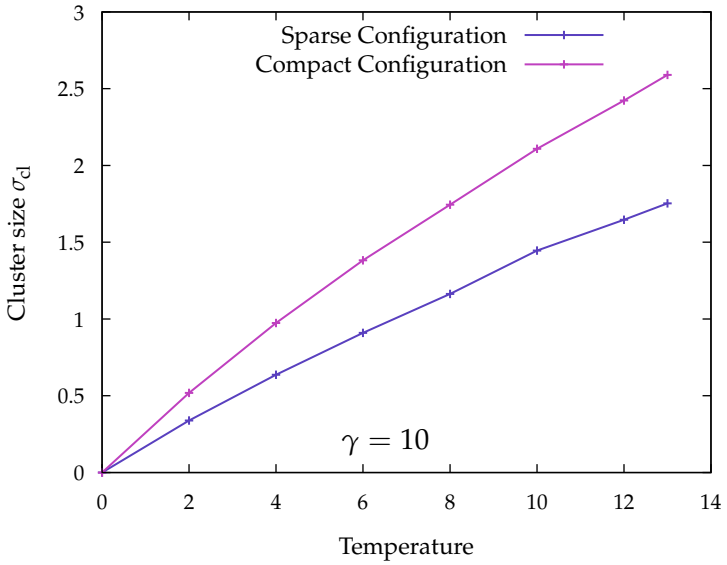

Figure 2.17: Cluster size $\sigma_c l$ as a function of temperature. Data obtained thanks to numerical simulations using parameters $N = 400$, $\mathcal{R}_c = 15$, $R_{\text{int}} = 3$, $v_0 = 10$, $\gamma = 10$; time-step $\Delta t = 0.01$; total elapsed time $t = 4000$.

Stability

As in the previous section, we must check if the phase transition is real or not. As expected, temperature T_{st} still exists finite even in this case (see table 2.3) and therefore system has a non continuos phase transition.

Friction Value	Stability Temperature	Critical Temperature
$\gamma = 1$	$15 \leq T_{\text{st}} \leq 16$	$13 \leq T_c \leq 14$
$\gamma = 10$	$14 \leq T_{\text{st}} \leq 15$	$13 \leq T_c \leq 14$

Table 2.3: Comparison between the stability temperature T_{st} and the critical temperature T_c. Data obtained thanks to numerical simulations using parameters $N = 400$, $\mathcal{R}_c = 15$, $R_{\text{int}} = 5$, $v_0 = 10$; time-step $\Delta t = 0.01$; total elapsed time $t = 4000$.

2.2.3 Infinite Interaction Range

Finally, we study the system dynamics in the extreme case where all particles interact with each other ($R_{\text{int}} = 2\mathcal{R}_c$).

The dynamics of this system ranges on a much bigger temperature range than in the previous cases. Indeed we can observe two peculiar features, not found in the finite interaction cases:

1. At high temperatures, the compact phase seems to split and form an additional *intermediate* phase, leading to the coexistence of three different spatial configurations (see fig. 2.18). Note, however, that the existence of this intermediate phase could be found only studying parameter σ_{cl}, while velocity magnetisation m and spatial entropy λ show no other configuration than the sparse and the compact one. Henceforth, this confirms that σ_{cl} is a particularly suitable parameter to study the emergence of peculiar spatial configurations.
2. The system undergoes not one, but three phase transitions. Indeed, in the finite interaction range case, system has a phase transition when the sparse configuration reaches a critical size $\sigma_{\text{cl}}^{(\text{sparse})} \sim \frac{1}{2}R_{\text{int}}$. Here, instead, if $T < T_c$, the system can always recover from a disordered state and returns in the rotation phase. Therefore, increasing temperature, first sparse phase undergoes a phase transition, followed by the intermediate one and finally by the compact one.

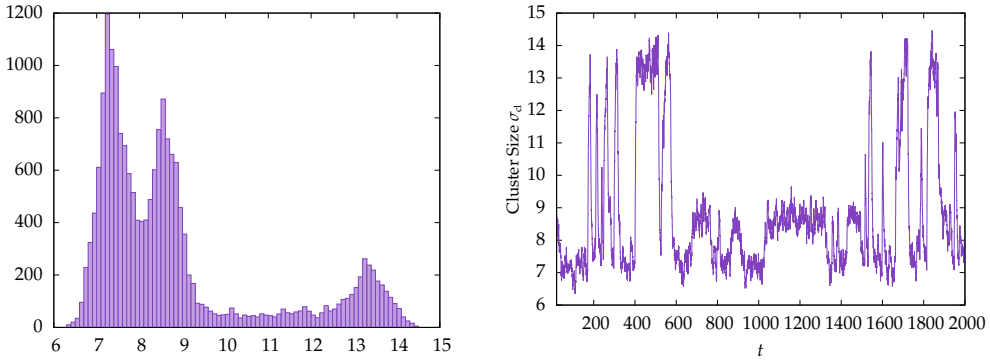

(a) Cluster Size σ_{cl} distribution

(b) Cluster Size σ_{cl} time evolution

Figure 2.18: Diagram showing the coexistence of three different phases when particles haven infinite interaction range

We fix the confining radius $\mathcal{R}_c$ to a value of $\mathcal{R}_c = 15$; the interaction range to $R_{\text{int}} = 2\mathcal{R}_c = 30$; the number of particles to $N = 400$; and the particles velocity to $v_0 = 10$. As usual, we will examine our system behaviour at low and high friction regimes.

Low Friction

We set friction coefficient to $\gamma = 1$.

Results show that the peculiar dynamics of the spatial configurations greatly differ at high temperatures (see figs. 2.19 and 2.20), characterised by great differences in th value of m and σ_{cl}. Indeed, system undergoes three different phase transitions, one for each phase: first the sparse phase ($T \sim 60$), than the intermediate one ($T \sim 75$) and lastly the compact one ($T \sim 80$).

At a first glance at fig. 2.19, we could guess that the rotating configurations have a continuous phase transition. However, cluster size trend (see fig. 2.20) shows that phase transition occurs when $\sigma_{\text{cl}} \sim \mathcal{R}_c$, this suggests that transition is still of the first order. Indeed, we could think that, in the limit of an infinite confining radius $\mathcal{R}_c$, the cluster dimension would still indefinitely grow.

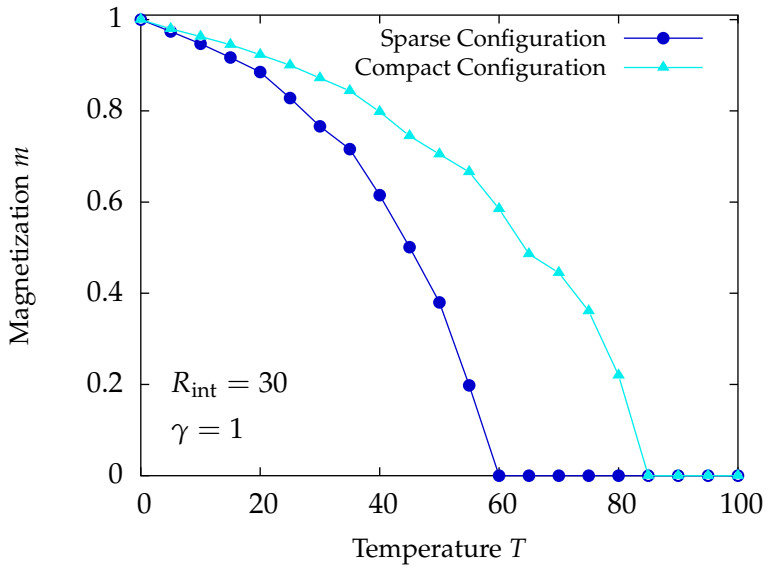

Figure 2.19: Reflecting-boundaries low-friction clustering transition. Data have been obtained as a time average after convergence to a stationary regime. Numerical parameters are: $\gamma = 10$; $N = 400$; $\mathcal{R}_c = 15$; $R_{\text{int}} = 30$; $v_0 = 10$; time-step $\Delta t = 0.01$; total elapsed time $t = 2000$.

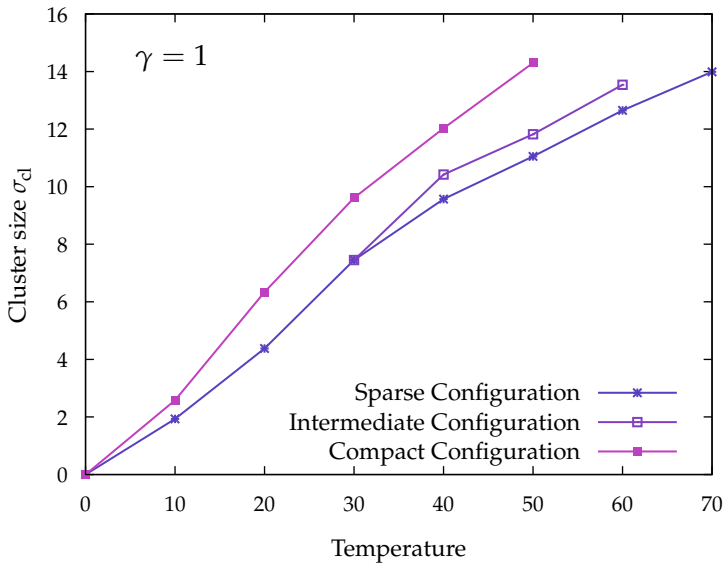

Figure 2.20: Cluster size $\sigma_c l$ as a function of temperature. Data obtained thanks to numerical simulations using parameters $N = 400$, $\mathcal{R}_c = 15$, $R_{\text{int}} = 3$, $v_0 = 10$, $\gamma = 11$; time-step $\Delta t = 0.01$; total elapsed time $t = 4000$.

High Friction

We increase friction coefficient to $\gamma = 10$. Results are similar to the ones in the previous case and can be seen in fig. 2.21. Note only that, as in section section 2.2.2, magnetisation is systematically higher than in the $\gamma = 1$ case and cluster size (see fig. 2.22) is systematically smaller.

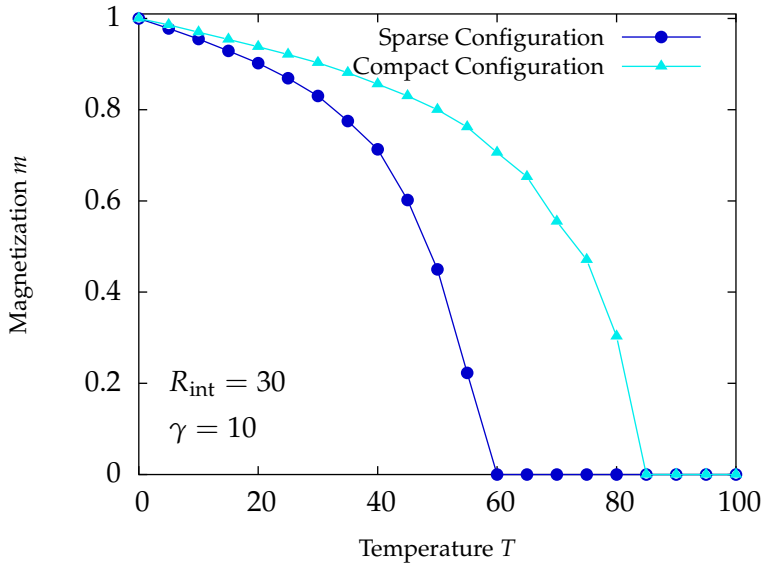

Figure 2.21: Reflecting-boundaries low-friction clustering transition. Data have been obtained as a time average after convergence to a stationary regime. Numerical parameters are: $\gamma = 10$; $N = 400$; $\mathcal{R}_c = 15$; $R_{\text{int}} = 30$; $v_0 = 10$; time-step $\Delta t = 0.01$; total elapsed time $t = 2000$.

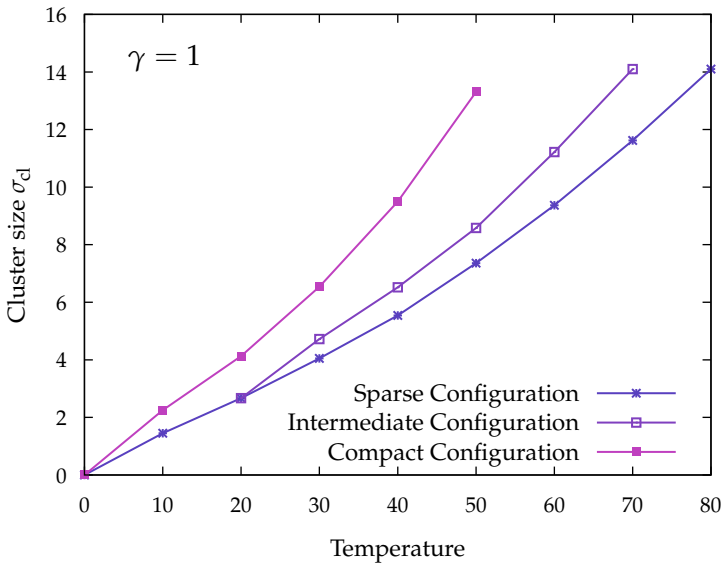

Figure 2.22: Cluster size $\sigma_c l$ as a function of temperature. Data obtained thanks to numerical simulations using parameters $N = 400$, $\mathcal{R}_c = 15$, $R_{\text{int}} = 3$, $v_0 = 10$, $\gamma = 10$; time-step $\Delta t = 0.01$; total elapsed time $t = 4000$.

CHAPTER 3

MOVING BOUNDARIES

As already mentioned, the continuous time version of the Vicsek model does not guarantee flock formation in domains without constraints. In this chapter we implement an alternative to the solution discussed in chapter 2, where individuals were forced to move in a still closed space and showed. We now drop such hypothesis and study the collective dynamics over longer times. Indeed, in this chapter we permit that particles can collectively move in any point of the space, but restricting each individual to not distance itself too much from the others. We imagine that particles are surrounded by a disk centred in their centre of mass, which, differently from the previous chapter, is not static and, instead, move accordingly the overall motion. On this moving disk, reflecting boundary conditions are implemented.

We will show that these simple constraint is sufficient to give rise to a variety of phenotypes which can be directly compared with the ones already mentioned in section 1.4. Indeed, while in chapter 2 only a rotating pattern would arise, here for example, particles can form a flock and move towards a direction or can alternate rotating around the centre of mass and moving towards a fixed direction.

3.1 THE MODEL

We consider a system of particles moving in a 2-dimensional space and surrounded by a disk of radius $\mathcal{R}_c$ centred in the centre of mass of the system. Particles are free to move inside the disk, but at the boundary, reflecting conditions are considered. Since this condition is difficult to implement numerically, in analogy to what already done in section 2.1, we introduce a confining potential depending on a constant K, such that, as $K \to \infty$, reflecting boundaries are recovered. Henceforth, equations (1.9) are recasted

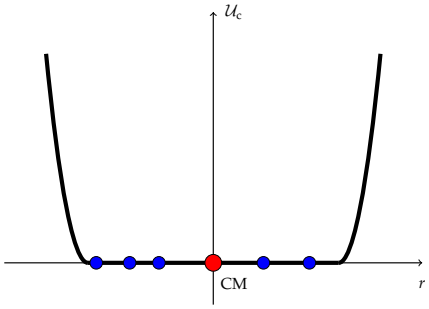

Figure 3.1: Form of potential $\mathcal{U}_c$, centred in the centre of mass (labelled with a red dot) of the particles (labelled with blue dots).

into:

$$\begin{cases} \dot{x}_i = v_0 \cos\theta_i \\ \dot{y}_i = v_0 \sin\theta_i \\ \dot{\theta}_i = \omega_i + \frac{1}{v_0} \sin(\theta - \phi_i^{\text{CM}}) \partial_{r_i} \mathcal{U}_c \left(r_i^{\text{CM}}\right) \\ \dot{\omega}_i = -\gamma\omega_i - \partial_{\theta_i} U + \sigma A_i \end{cases} , \tag{3.1}$$

where $\phi_i^{\text{CM}} = \text{atan}\left(\frac{y_i - y_{\text{CM}}}{x_i - x_{\text{CM}}}\right)$, $r_i^{\text{CM}} = \sqrt{(x_i - x_{\text{CM}})^2 + (y_i - y_{\text{CM}})^2}$ and:

$$x_{\text{CM}} = \frac{1}{N} \sum_{i=1}^{N} x_i \qquad\qquad y_{\text{CM}} = \frac{1}{N} \sum_{i=1}^{N} y_i \ ,$$

are the coordinates of the centre of mass. In analogy to (2.1) and due to its simple form, we choose an half-harmonic confining potential:

$$\mathcal{U}_c \left(r_i^{\text{CM}}\right) = \frac{1}{2} K \left(r_i^{\text{CM}} - \mathcal{R}_c\right)^2 \text{H}\left(r_i^{\text{CM}} - \mathcal{R}_c\right) \ . \tag{3.2}$$

3.2 Numerical Simulations

Numerical simulations show that these moving boundaries give rise to richer phenomenology than the one observed in chapter 2. Indeed, particles show three main dynamical behaviours:

1. particles tend to align and go along in the same direction; we will call this behaviour *travelling phase*;
2. particles form two (or, rarely, more) clusters and rotate around their centre of mass, we will call this behaviour *rotating phase*;
3. particles do not show coherent motion, we will call this behaviour *disordered phase*.

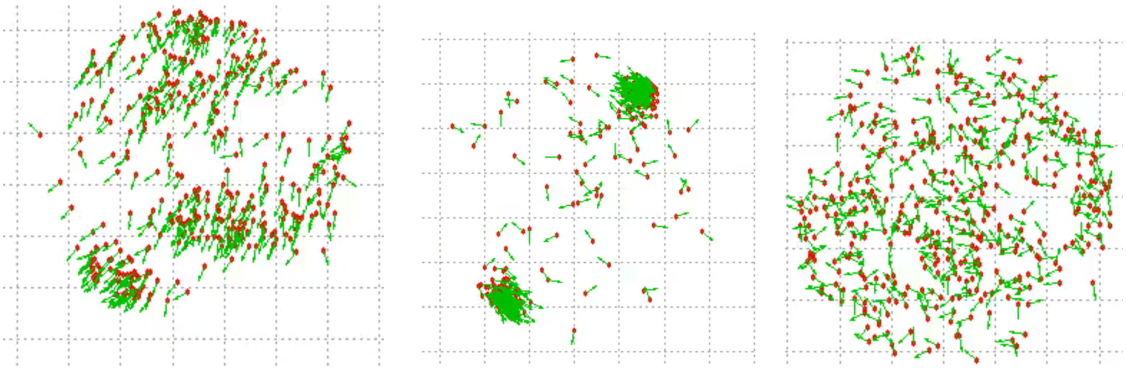

(a) Travelling Phase

(b) Rotating Phase

(c) Disordered Phase

Figure 3.2: Some Phases

Among the ordered phases arise, the *travelling* one is the most frequent, while the rotating one arises only for particular values of T and γ. conditions. At sufficiently low temperature, the travelling phase is characterised by high coherent motion, with particles moving altogether towards a certain direction. This behaviour closely resembles flocks of migrating birds (phenotype (c), displayed in section 1.4). Travelling flocks takes no preferred direction, thus we assume the existence of a rotating symmetry breaking phenomenon. If we increase the temperature, i.e. if we increase environmental noise, the travelling phase dynamics show often fast and synchronised changes of direction and the overall collective motion is, as expected, less coherent than before. This collective motion resembles the one displayed by swarms of insects (phenotype (a), displayed in section 1.4).

In chapter 2, we observed that there exists two different rotating phase, associated to difference in size of the rotating clusters. As in that case, here at fixed temperature T, we can observe the coexistence of two different travelling phases, characterised by different values of velocity magnetisation m. However, we can not associate these two phase to their spatial dynamics.

In the reflecting and the periodic boundaries conditions cases examined in the previous chapters, we found no substantial difference in the dynamics of the system when examining the low friction and the high friction regimes. In this case, instead, the angular friction coefficient value γ deeply influences the dynamics of the rotating phase. Indeed in the low friction regime the rotating phase arise only at high temperature, while at high friction regime it arises only at low temperatures (see fig. 3.3). The rotating phase closely resembles the dynamical patterns observed sometimes in shoals of fishes (phenotype (b) in section 1.4).

We now fix the confining constant K to a value of $K = 1000$; the confining radius to $\mathcal{R}_c = 15$; the interaction range to $R_{\text{int}} = 3$; the number of particles to $N = 400$; particles velocity to $v_0 = 10$. We, as usual, examine the system in the low and high friction regimes.

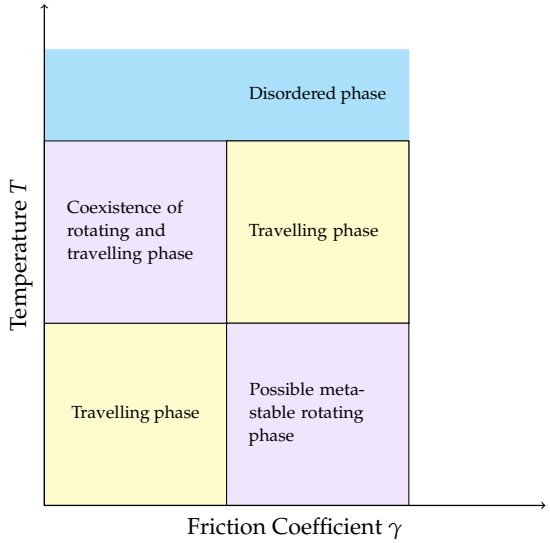

Figure 3.3: Illustrative phase diagram showing the emergence of the three phases varying friction coefficient and temperature.

Low Friction Regime

In this case we the fix friction coefficient to $\gamma = 1$.

System show a complex dynamics, strongly dependent on the temperature. Results are summarised in the following table:

Temperature	**Dynamic**
$T < 3$	Travelling phase is dominant. No other phases are observed.
$3 \lesssim T \lesssim 3.5$	Travelling phase is the most probable. Sometimes we observe that particles at first are in the rotating phase, but after a while change their behaviour and can be observed in the travelling phase. They do not show rotating behaviour anymore.
$3.5 \lesssim T \lesssim 5$	System show a coexistence between the rotating and the travelling phase (see fig. 3.4).
$5 \lesssim T \lesssim 6$	There is a coexistence between the rotating and the disordered phase.
$T \gtrsim 6$	Only disordered phase is observed.

By observing the profiles in fig. 3.5 we have that, when travelling phase arises, system seems to undergo two phase transitions ($T \lesssim 5$), one for each configurations. We will conventionally call these configurations *coherent* and *incoherent* phases. We are not certain of the nature of such transition. However, by remembering results obtained in the

periodic boundaries condition case (see section 1.7), we suggest that what observed is indeed a continuous phase transition.

Spatial pattern dynamics depends on the phase. In travelling phase system show cluster formation only at really low temperatures ($T \lesssim 0.5$), while at higher temperatures particles are homogeneously distributed in space. Rotating phase, instead, show strong spatial coherence with the formation of two small clusters which rotates around the centre of mass.

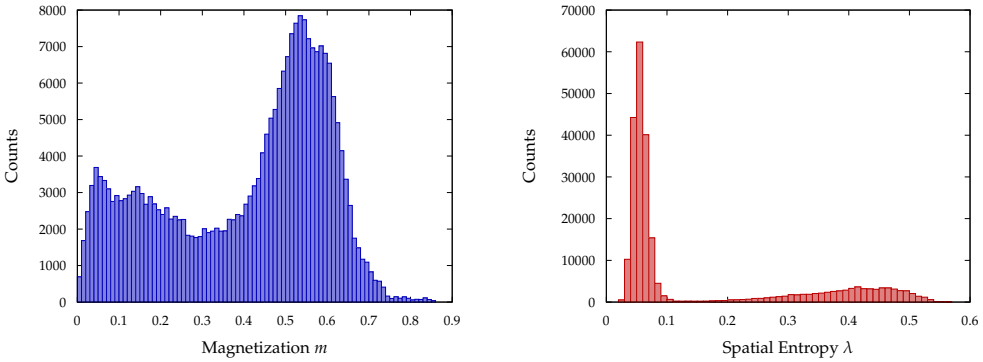

(a) Velocity Magnetisation m **(b)** Spatial Entropy λ

Figure 3.4: These histograms gives evidence of the coexistence of two phases. In fig. 3.4a the low magnetisation peak is associated to the rotating phase, while the other one is due to the travelling phase. Since travelling phase show low spatial coherence, in fig. 3.4b the first peak is associated to the travelling phase, while the second, due to the presence of several clusters, is associated to the rotational phase. Numerical parameters used in the simulation: $N = 400$; $\mathcal{R}_c = 15$; $R_{\text{int}} = 3$; $\gamma = 1$; $v_0 = 10$; $T = 4$. Integration have been performed using a time-step $\Delta t = 0.01$ for a time of $t = 4000$.

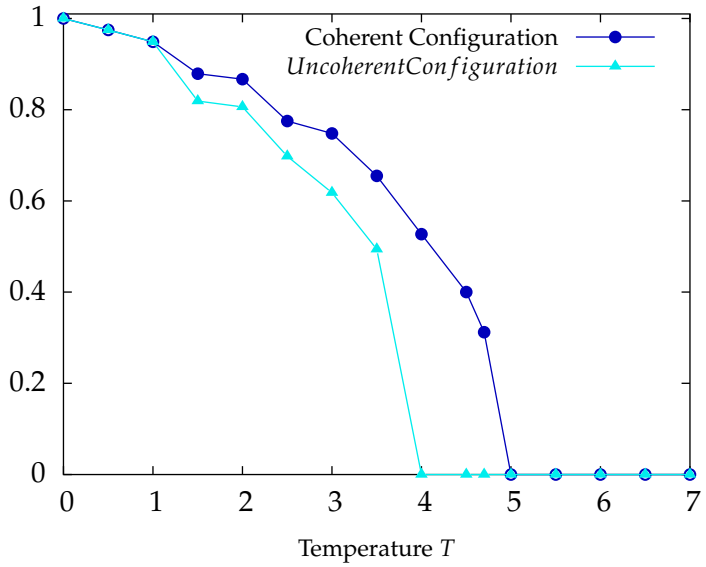

Figure 3.5: Velocity magnetisation m as a function of Temperature, when travelling behaviour arise. $N = 400$; $\mathcal{R}_c = 15$; $R_{\text{int}} = 3$; $\gamma = 1$; $v_0 = 10$. Data obtained with numerical simulations using a time-step of $\Delta t = 0.01$ for a time of $t = 4000$.

High Friction Regime

Here we raise friction coefficient to $\gamma = 10$.

During travelling phase, particles behave similar as in the low friction case. However it is really difficult to distinguish between the coherent and the incoherent phase, since their typical magnetisation values appear to be closer than in the previous case. Therefore in fig. 3.6 we can only observe a mean magnetisation value between these two configurations.

Rotating phase can only be observed at low temperatures ($T \lesssim 3$) and, differently from the low friction regime case, such phase appears to be stable. Its appearance is random: at a fixed temperature T we can both have travelling (most probable) and rotating phase (less probable). This is probably due to the starting conditions of the system.

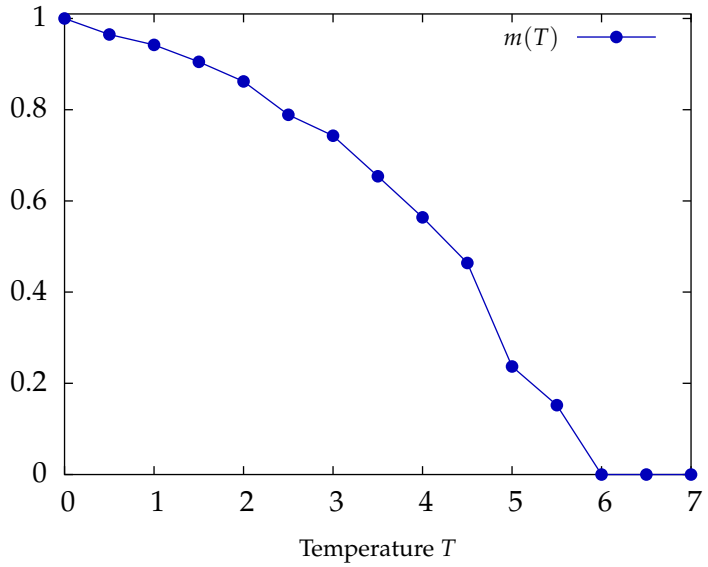

Figure 3.6: Velocity magnetisation m as a function of Temperature, when aligning behaviour arise. $N = 400$; $\mathcal{R}_c = 15$; $R_{\text{int}} = 3$; $\gamma = 1$; $v_0 = 10$.Data obtained with numerical simulations using a time-step of $\Delta t = 0.01$ for a time of $t = 4000$.

CONCLUSIONS

In this thesis we have defined a model for the description of collective motion in a system of active units with interactions depending on their relative positions. The system has been extensively studied in domains with different boundary conditions and in the simple case of point-like particles.

First we examined a system composed of N particles moving in a square with periodic boundary conditions. Numerical results show that in this case particles tend to quickly align and move altogether toward a certain direction. The system seems to undergo a continuous phase transition, between an ordered phase characterised by coherent motion and a disordered one characterised by incoherent motion. Note that this result was expected in the light of previous works on the Vicsek model. Spatial dynamics is strongly dependent on the angular friction coefficient parameter γ. Indeed, in the low friction regime we observed the formation of small, high density, flocks, while in the high friction regime we could not observe spatial coherence within such setup. Our system can be mapped onto the Hamiltonian Mean Field model if the particles density is homogeneous. Indeed, in the high friction regime we could observe a great accordance between analytical predictions and numerical simulations.

Secondly, the model has been tested in a confined domain. Within this context, particles are bound to move in a disk with reflecting boundary conditions at border, and their dynamics change dramatically from the previous case. Numerical simulations show that at low temperatures, particles quickly gather in a unique small cluster which rotates along the border. The system still undergoes a phase transition from an ordered phase, characterised by the rotating state, and a disordered one, but this time transition is of the first order. The rotating steady state can be predicted analytically, but it is not completely clear why it is an attractor at low temperatures. Note that rotating behaviours are typical of spatial constrained active-matter systems, suggesting possible applications for our model.

With this boundary conditions, reveals our model problematic traits. Indeed, the phase transition only occurs when the rotating cluster reaches size comparable with the interaction range R_{int}. This suggests that the cluster is stable only if all particles are interacting with each other. However this, in a model employing particles with non-null size, can not occur for reasonable values of R_{int}. Therefore we suppose that if we consider particles with exclusive volume, our model has to be extended adding an effective attractive potential between particles.

Lastly, we considered our model when particles are bound to move inside a moving disk, centred in their centre of mass. Such a constraint permits the emergence of travelling states, which were impossible in the previous case. The system shows indeed three possible states: a travelling state, where particles do not form clusters, but do move altogether towards a certain direction; a rotating state, where particles form two clusters and rotates around the centre of mass; a disordered state, where particles show incoherent motion. Henceforth, we can observe a much richer phenomenology than before, which closely resembles what observed in nature. The emergence of a certain state in a system, seems to be strongly dependent on the temperature T and angular friction γ values. However, from our simulations it is difficult to determine the minimal conditions needed to give rise to a certain state. Henceforth, further numerical studies are needed to fully disclose the dynamics of this system.

"So long and thanks for all the fish."

Douglas Adams, `The Hitchhiker's Guide to the Galaxy`

APPENDIX A

HMF EQUILIBRIUM

In this section we will study the equilibrium properties of a system described by a generalized version of Hamiltonian (1.24), coupled with a termal bath with temperature T. This system is described within the canonical ensemble, where all the relevant observables are derived through the partition function $\mathcal{Z}$. We assume the Hamiltonian is in the form:

$$H = \frac{1}{2}\sum_{i=1}^{N}\omega_i^2 + \frac{K}{2N}\sum_{i=1}^{N}\sum_{j=1}^{N}\left[1-\cos\theta_i-\theta_j\right] + \sum_{i=1}^{N}\left(h_1\cos\theta_i + h_2\sin\theta_i\right) \quad , \tag{A.1}$$

where K is a coupling constant and $\vec{h} = (h_1, h_2)^t$ is a constant external field.

It is useful to introduce, in analogy to (1.16), the magnetization vector:

$$\vec{m} = \frac{1}{N}\left(\sum_{i=1}^{N}\cos\theta_i,\ \sum_{i=1}^{N}\sin\theta_i\right)^t \quad . \tag{A.2}$$

It can be proven that the following trigonometric equation holds:

$$\sum_{j=1}^{N}\left[1-\cos\theta_i-\theta_j\right] = N^2 - \left(\sum_{i=1}^{N}\cos\theta_i\right)^2 - \left(\sum_{i=1}^{N}\sin\theta_i\right)^2 = N^2(1-m^2) \quad .$$

Hence, we can rewrite (A.1) as

$$H = \frac{1}{2}\sum_{i=1}^{N}\omega_i^2 + \frac{KN}{2}(1-m^2) + N\vec{m}\cdot\vec{h} \quad . \tag{A.3}$$

We can finally start the computation of the partition function in a canonical ensemble at fixed temperature T.

$$\begin{aligned}\mathcal{Z} &= \int_{\mathbb{R}^N\times\mathbb{T}^N} e^{-\beta H}\prod_{i=1}^{N}(\,\mathrm{d}\omega_i\,\mathrm{d}\theta_i) \\ &= \left(\prod_{i=1}^{N}\int_{\mathbb{R}}\exp\left[-\frac{\beta}{2}\omega_i^2\right]\,\mathrm{d}\omega_i\right)\int_{\mathbb{T}^N}\mathrm{d}\theta_1\ldots\mathrm{d}\theta_N\,\exp\left[-\frac{\beta KN}{2}\left(1-m^2+2\vec{m}\cdot\frac{\vec{h}}{K}\right)\right]\end{aligned} \tag{A.4}$$

Integration over ω_i is trivial, therefore partition function is recast into:

$$\begin{aligned}\mathcal{Z} &= \left(\frac{2\pi}{\beta}\right)^{\frac{N}{2}} \int_{\mathbb{T}^N} \mathrm{d}\theta_1 \dots \mathrm{d}\theta_N \, \exp\left[-\frac{\beta K N}{2}\left(1 - m^2 + 2\vec{m}\cdot\frac{\vec{h}}{K}\right)\right] \\ &= \left(\frac{2\pi}{\beta} e^{-\beta-\beta\frac{h^2}{K^2}}\right)^{\frac{N}{2}} \int_{\mathbb{T}^N} \mathrm{d}\theta_1 \dots \mathrm{d}\theta_N \, \exp\left[\frac{\beta K N}{2}\left(m^2 - 2\vec{m}\cdot\frac{\vec{h}}{K} + \frac{h^2}{K^2}\right)\right]\end{aligned} \tag{A.5}$$

We now define the Hubbard-Stratonovich transform, for all $\vec{v} \in \mathbb{R}^2$ holds the following equality:

$$e^{\alpha v^2} = \frac{1}{\pi}\int_{\mathbb{R}^2} e^{-(w^2 + 2\sqrt{\alpha}\vec{w}\cdot\vec{v})}\,\mathrm{d}w_x\,\mathrm{d}w_y \ . \tag{A.6}$$

Applying this transform to partition function $\mathcal{Z}$, we have that:

$$\begin{aligned}\mathcal{Z} &= \frac{1}{\pi}\left(\frac{2\pi}{\beta} e^{-\beta-\beta\frac{h^2}{K^2}}\right)^{\frac{N}{2}} \int_{\mathbb{R}^2} \mathrm{d}w_x\,\mathrm{d}w_y \int_{\mathbb{T}^N} \mathrm{d}\theta_1 \dots \mathrm{d}\theta_N e^{-\left(w^2 + \sqrt{2\beta K N}\vec{w}\cdot(\vec{m}+\frac{\vec{h}}{K})\right)} \\ &= \frac{1}{\pi}\left(\frac{2\pi}{\beta} e^{-\beta-\beta\frac{h^2}{K^2}}\right)^{\frac{N}{2}} \int_{\mathbb{R}^2} \mathrm{d}w_x\,\mathrm{d}w_y e^{-w^2 - \sqrt{2\beta K N}\vec{w}\cdot\frac{\vec{h}}{K}} \prod_{i=1}^{N}\int_{\mathrm{S}^1} e^{-\sqrt{\frac{2\beta K}{N}}(w_x\cos\theta_i + w_y\sin\theta_i)}\,\mathrm{d}\theta_i\end{aligned}$$

Let us now define the angle $\phi = \operatorname{atan}\frac{w_y}{w_x}$, then :

$$\begin{aligned}\int_{\mathrm{S}^1} e^{-\sqrt{\frac{2\beta K}{N}}(w_x\cos\theta + w_y\sin\theta)}\,\mathrm{d}\theta &= \int_0^{2\pi} e^{-\sqrt{\frac{2\beta K}{N}} w\cos(\theta-\phi)}\,\mathrm{d}\theta \\ &= 2\pi I_0\left(\sqrt{\frac{2\beta K}{N}} w\right)\end{aligned}$$

It is now useful to define $\vec{w}' = \sqrt{\frac{2\beta K}{N}}\vec{w}$, than partition function become:

$$\mathcal{Z} = \frac{N}{2\pi\beta K}\left(\frac{2\pi}{\beta} e^{-\beta-\beta\frac{h^2}{K^2}}\right)^{\frac{N}{2}} \int_{\mathbb{R}^2} \mathrm{d}w'_x\,\mathrm{d}w'_y e^{-N\left(\frac{w'^2}{2\beta K} - \vec{w}'\cdot\frac{\vec{h}}{K} - \log(2\pi\, I_0(w'))\right)} \tag{A.7}$$

This last integral cannot be computed exactly, we shall then use a saddle point approximation for the calculation of the finite size free energy F_N:

$$\begin{aligned}F_N = -\tfrac{1}{\beta}\log\mathcal{Z} = -\tfrac{1}{\beta}\log\left(\tfrac{N}{2\pi\beta K}\right) - \tfrac{N}{2\beta}\log\left(\tfrac{2\pi}{\beta}\right) + \tfrac{N}{2}\left(1 + \tfrac{h^2}{K^2}\right) + \\ + \tfrac{N}{\beta}\min_{w\in\mathbb{R}^2}\left[\tfrac{w^2}{2\beta K} - \tfrac{\vec{h}}{K}\cdot\vec{w} - \log(2\pi I_0(w))\right]\end{aligned} \tag{A.8}$$

In the thermodynamical limit, free energy per particle $f \equiv \frac{F_N}{N}$ is:

$$\begin{aligned}f = \lim_{N\to\infty}\tfrac{F_N}{N} = -\tfrac{1}{2\beta}\log\left(\tfrac{2\pi}{\beta}\right) + \tfrac{1}{2}\left(1 + \tfrac{h^2}{K^2}\right) + \\ + \tfrac{1}{\beta}\min_{w\in\mathbb{R}^2}\left[\tfrac{w^2}{2\beta K} - \tfrac{\vec{h}}{K}\cdot\vec{w} - \log(2\pi I_0(w))\right]\end{aligned} \tag{A.9}$$

Let us now find the value $w^\star$ which minimize the expression in the parenthesis in the equation above when $\vec{h} = 0$. We must solve the equations:

$$\frac{d}{dw}\left[\frac{w^2}{2\beta K} - \log(2\pi I_0(w))\right] = \frac{w}{\beta K} - \frac{I_1(w)}{I_0(w)} \tag{A.10}$$

$$\frac{d^2}{dw^2}\left[\frac{w^2}{2\beta K} - \log(2\pi I_0(w))\right] = \frac{1}{\beta K} - \frac{1}{2} - \frac{I_2(w)}{2I_0(w)} - \frac{I_1(w)^2}{I_0(w)^2} > 0 \tag{A.11}$$

Equation (A.10) usually have three or one solutions, including the trivial one $w = 0$. To check if the null solution is actually a minimum we employ condition (A.11); we have that:

$$\frac{d^2}{dw^2}\left(\frac{w^2}{2\beta K} - \log(2\pi I_0(w))\right|_{w=0} = \frac{1}{\beta K} - \frac{1}{2} \ . \tag{A.12}$$

Henceforth $w = 0$ is a minimum if and only if $T > \frac{K}{2}$, while if $T < \frac{K}{2}$ the null solution is a maximum and the function is minimized by a $w^\star \neq 0$.

We now conclude finding the mean magnetization m and the energy per particle at the equilibrium. It is easily proven that:

$$m = \left(\frac{\partial f}{\partial \vec{h}}\right|_{\vec{h}=0} = \frac{w^\star}{\beta K} \ , \tag{A.13}$$

where $w^\star$ is a solution of equations (A.10) and (A.11). Using equation (A.10) we get an implicit equation for m:

$$m = \frac{I_1(m\beta K)}{I_0(m\beta K)} \tag{A.14}$$

We have then that $m = 0$ if $T > \frac{K}{2}$ and $m \neq 0$ if $T < 0.5$. Numerical solutions show that the magnetization has a second order phase transition with critical temperature $T = \frac{K}{2}$.

Energy per particle e can also be found as a derivative of f:

$$\frac{\partial}{\partial \beta}(\beta f) = \frac{1}{2}\left(K(1 - m^2) + \frac{1}{\beta}\right) \tag{A.15}$$

APPENDIX B

NUMERICAL METHODS

We consider a system of N, moving in a two dimensional space, whose continuous motion is described by equations (1.13). To study the system with numerical means, we use a conventional two-step velocity-Verlet algorithm. At each time-step the integration scheme is the following. Firstly, the positions and the directions are updated of one time-step Δt, while ω_i is updated only of half time-step:

$$\begin{cases} x_i(t+\Delta t) = x_i(t) + v_0 \cos\theta_i \Delta t \\ y_i(t+\Delta t) = y_i(t) + v_0 \sin\theta_i \Delta t \\ \theta_i(t+\Delta t) = \theta_i(t) + \omega_i(t)\Delta t + \mathcal{F}_i(t)\frac{\Delta t^2}{2} + \frac{2}{3}\sqrt{2\gamma T}\Delta W_i(t)\Delta t^{\frac{3}{2}} \\ \omega_i(t+\frac{1}{2}\Delta t) = \omega_i(t) + \mathcal{F}_i(t)\frac{\Delta t}{2} + \sqrt{2\gamma T}\Delta W_i(t)\sqrt{\frac{\Delta t}{2}} \end{cases} , \tag{B.1}$$

where:

$$\mathcal{F}_i(t) = -\gamma\omega_i(t) - \sum_{j=1}^{N} \sin\left(\theta_i(t) - \theta_j(t)\right) \mathrm{H}\left(R_{\mathrm{int}} - \left\|\vec{r}_i - \vec{r}_j\right\|\right) \ . \tag{B.2}$$

Secondly, $\mathcal{F}_i$ is calculated at the time $t+\Delta t$ by using $x_i(t+\Delta t)$, $\theta_i(t+\Delta t)$ and $\omega_i(t+\frac{\Delta t}{2})$. Finally, the update of ω_i is completed:

$$\omega_i(t+\Delta t) = \omega_i(t+\tfrac{\Delta t}{2}) + \mathcal{F}_i(t+\Delta t)\tfrac{\Delta t}{2} + \sqrt{2\gamma T}\Delta W_i(t+\Delta t)\sqrt{\tfrac{\Delta t}{2}} \tag{B.3}$$

APPENDIX C

FOKKER PLANCK EQUATIONS FOR THE CTVM

C.1 FOKKER FOR HMF

We want to compute the Fokker-Planck equation, describing the approach to equilibrium of Hamiltonian (1.24). We start by writing the Langevin equations:

$$\begin{cases} \dot{\theta}_i = \omega_i \\ \dot{\omega}_i = -\gamma\omega_i - \frac{K}{N}\sum_{j=1}^{N}\sin(\theta_i - \theta_j) + \sqrt{2\gamma T}A_i(t) \end{cases} . \tag{C.1}$$

We now compute the Kramers-Moyal coefficients from eqs. (C.1).

- Drift coefficients, eqreferred to a quantity x, are defined as:

$$D_i^{(x)} = \lim_{\Delta t\to 0}\frac{1}{\Delta t}\langle x_i(t+\Delta t) - x_i(t)\rangle \tag{C.2}$$

  Hence a simple computation gives us that:

$$D_i^{(\theta)} = \omega_i(t) \qquad D_i^{(\omega)} = -\gamma\omega_i(t) - \frac{K}{N}\sum_{j=1}^{N}\sin\left(\theta_i - \theta_j\right) \tag{C.3}$$

- Diffusions coefficient of variables x and y are defined as:

$$\mathcal{D}_{ij}^{(x,y)} = \frac{1}{2}\lim_{\Delta t\to 0}\frac{1}{\Delta t}\langle (x_i(t+\Delta t) - x_i(t))\,(y_i(t+\Delta t) - y_i(t))\rangle \tag{C.4}$$

  It is easy to prove that every diffusion coefficient is null, with the exception of:

$$\mathcal{D}_{ij}^{(\omega,\omega)} = \mathfrak{D}\delta_{ij} \tag{C.5}$$

  where $\mathfrak{D} = \gamma T$.

Therefore Fokker-Planck equation for the probability density function of N particles is:

$$\partial_t p_N(\theta_1,\dots,\theta_N;\omega_1,\dots,\omega_N;t) = \sum_{i=1}^{N}\left[-\partial_{\theta_i}D_i^{(\theta)} - \partial_{\omega_i}D_i^{(\omega)} + \partial^2_{\omega_i}\mathcal{D}_{ij}^{(\omega,\omega)}\right] p_N \tag{C.6}$$

Using (C.5) and (C.3) we have that:

$$\partial_t p_N = \sum_{i=1}^{N}\left[-\omega_i\partial_{\theta_i} + \partial_{\omega_i}\left(\gamma\omega_i + \mathfrak{D}\partial_{\omega_i}\right) + \frac{K}{N}\sum_{i=1}^{N}\sin(\theta_i-\theta_j)\partial_{\omega_i}\right] p_N \tag{C.7}$$

To obtain an expression for the single particle density function p_1, we have to marginalise equation (C.7) integrating over variables $\theta_1,\dots,\theta_{N-1}$ and $\omega_1,\dots,\omega_{N-1}$. The first term in (C.7) on the right hand side becomes:

$$\sum_{i=1}^{N}\int_{\mathbb{T}^{N-1}}\mathrm{d}\theta_2\cdots\mathrm{d}\theta_N\int_{\mathbb{R}^{N-1}}\mathrm{d}\omega_2\cdots\mathrm{d}\omega_N\ \omega_i\partial_{\theta_i}p_N = \omega_1\partial_{\theta_1}p_1(\theta_1,\omega_1,t)\ , \tag{C.8}$$

since the integration over $\mathbb{S}^1$ of the angular derivative $\partial_\theta p_N$ gives always zero. Furthermore, if we use the physical assumption that $\omega_i p_N \to 0$, $\partial_{\omega_i}p_N \to 0$ as $\omega_i \to \pm\infty$, we have that the second term in (C.7) becomes:

$$\begin{aligned}\sum_{i=1}^{N}\int_{\mathbb{T}^{N-1}}\mathrm{d}\theta_2\cdots\mathrm{d}\theta_N\int_{\mathbb{R}^{N-1}}\mathrm{d}\omega_2\cdots\mathrm{d}\omega_N\,\partial_{\omega_i}\left(\gamma\omega_i+\mathfrak{D}\partial_{\omega_i}\right)p_N = \\ \partial_{\omega_1}\left(\gamma\omega_1+\mathfrak{D}\partial_{\omega_1}\right)p_1(\theta_1,\omega_1,t)\end{aligned} \ . \tag{C.9}$$

Last term is, instead, more problematic; we have that:

$$\begin{aligned}\frac{K}{N}\sum_{i,j=1}^{N}\int_{\mathbb{T}^{N-1}}\mathrm{d}\theta_2\cdots\mathrm{d}\theta_N\int_{\mathbb{R}^{N-1}}\mathrm{d}\omega_2\cdots\mathrm{d}\omega_N\ \sin(\theta_i-\theta_j)\partial_{\omega_i}p_N = \\ K\partial_{\omega_1}\int_{\mathbb{T}\times\mathbb{R}}\mathrm{d}\theta'\,\mathrm{d}\omega' p_2(\theta_1,\omega_1,\theta',\omega',t)\sin(\theta'-\theta_1)\end{aligned} \ . \tag{C.10}$$

We finally resort to the mean field approximation where $p_2(\theta_1,\omega_1,\theta_2,\omega_2,t) = p_1(\theta_1,\omega_1,t)p_1(\theta_2,\omega_2,t)$. With this approximation Fokker-Planck equation is:

$$\partial_t p_1(\theta,\omega,t) = -\omega\partial_\theta p_1 + \partial_\omega(\gamma\omega p_1 + \partial_\omega p_1) + K\partial_\omega p_1\phi^{\mathrm{HMF}}(\theta,t) \tag{C.11}$$

Where:

$$\phi^{\mathrm{HMF}}(\theta,t) = \int_{\mathbb{T}\times\mathbb{R}}\mathrm{d}\theta'\,\mathrm{d}\omega' p_1(\theta',\omega',t)\sin(\theta-\theta') \tag{C.12}$$

C.2 FOKKER FOR CTVM PERIODIC

We now look for the Fokker-Planck equation associated to equations eq. (1.13). Procedure is really similar to what done in the previous section. Fokker-Planck equation for the N

particles density function is:

$$\partial_t p_N = \sum_{i=1}^{N} \left[-v_0 \cos\theta_i \partial_{x_i} - v_0 \sin\theta_i \partial_{y_i} - \omega_i \partial_{\theta_i} + \partial_{\omega_i} \left(\gamma\omega_i + \mathfrak{D}\partial_{\omega_i} \right) + \frac{K}{N} \sum_{i=1}^{N} \sin(\theta_i - \theta_j) \partial_{\omega_i} \right] p_N \tag{C.13}$$

Note that p_N now depends also on spatial coordinates. Marginalising this equation and using that p_N is null for $x_i \to \infty$ or $y_i \to \infty$, we have that:

$$\partial_t p_1 = -v_0 \cos\theta \partial_x p_1 - v_0 \sin\theta \partial_y p_1 - \omega \partial_\theta p_1 + \partial_\omega \left(\gamma\omega + \mathfrak{D}\partial_\omega \right) p_1 + N \partial_\omega \Xi(\vec{x}, \theta, \omega, t) \tag{C.14}$$

where:

$$\Xi(\vec{x}, \theta, \omega, t) = \int_{\mathbb{T}\times\mathbb{R}\times\mathbb{R}^2} \mathrm{d}\theta' \, \mathrm{d}\omega' \, \mathrm{d}\vec{x}' \, \sin(\theta - \theta') p_2(\theta, \omega, \vec{x}, \theta', \omega', \vec{x}', t) \mathrm{H}\left(R_{\text{int}} - \left\| \vec{x} - \vec{x}' \right\| \right) \tag{C.15}$$

Ore, if we use a mean field approximation:

$$\partial_t p_1 = -v_0 \cos\theta \partial_x p_1 - v_0 \sin\theta \partial_y p_1 - \omega \partial_\theta p_1 + \partial_\omega \left(\gamma\omega + \mathfrak{D}\partial_\omega \right) p_1 + N \partial_\omega p_1 \Phi(\theta, t) \tag{C.16}$$

Where:

$$\Phi(\theta, t) = \int_{\mathbb{T}\times\mathbb{R}\times\mathbb{R}^2} \mathrm{d}\theta' \, \mathrm{d}\omega' \, \mathrm{d}\vec{x}' \, \sin(\theta - \theta') p_1(\theta', \omega', \vec{x}', t) \mathrm{H}\left(R_{\text{int}} - \left\| \vec{x} - \vec{x}' \right\| \right) \tag{C.17}$$

Bibliography

[1] S. Ramaswamy, "The mechanics and statistics of active matter," *Annu. Rev. Condens. Matter Phys.*, vol. 1, pp. 323–345, aug 2010.

[2] A. Czirók, E. Ben-Jacob, I. Cohen, and T. Vicsek, "Formation of complex bacterial colonies via self-generated vortices," *Phys. Rev. E*, vol. 54, pp. 1791 – 1801, Aug 1996.

[3] J. H. Ingmar H. Riedel, Karsten Kruse, "A self-organized vortex array of hydrodynamically entrained sperm cells," *Science*, vol. 309, pp. 300–305, 2005.

[4] F. J. Ndlec, T. Surrey, A. C. Maggs, and S. Leibler, "Self-organization of microtubules and motors," *Nature*, vol. 389, pp. 305–308, Sep 1997.

[5] A. Okubo and S. Levin, *Diffusion and Ecological Problems: Modern Perspectives*. Interdisciplinary Applied Mathematics, Springer New York, 2002.

[6] A. Czirók and T. Vicsek, "Collective behavior of interacting self-propelled particles," *Physica A: Statistical Mechanics and its Applications*, vol. 281, no. 1–4, pp. 17 – 29, 2000.

[7] Chaté, H., Ginelli, F., Grégoire, G., Peruani, F., and Raynaud, F., "Modeling collective motion: variations on the vicsek model," *Eur. Phys. J. B*, vol. 64, no. 3-4, pp. 451–456, 2008.

[8] A. Bricard, J.-B. Caussin, N. Desreumaux, O. Dauchot, and D. Bartolo, "Emergence of macroscopic directed motion in populations of motile colloids," *Nature*, vol. 503, pp. 95–98, nov 2013.

[9] A. Kudrolli, G. Lumay, D. Volfson, and L. S. Tsimring, "Swarming and swirling in self-propelled polar granular rods," *Phys. Rev. Lett.*, vol. 100, p. 058001, Feb 2008.

[10] Y. Sumino, K. H. Nagai, Y. Shitaka, D. Tanaka, K. Yoshikawa, H. Chaté, and K. Oiwa, "Large-scale vortex lattice emerging from collectively moving microtubules," *Nature*, vol. 483, pp. 448–452, mar 2012.

[11] M. Poujade, E. Grasland-Mongrain, A. Hertzog, J. Jouanneau, P. Chavrier, B. Ladoux, A. Buguin, and P. Silberzan, "Collective migration of an epithelial monolayer in response to a model wound," *Proceedings of the National Academy of Sciences*, vol. 104, pp. 15988–15993, sep 2007.

[12] E. Lushi, H. Wioland, and R. E. Goldstein, "Fluid flows created by swimming bacteria drive self-organization in confined suspensions," *Proceedings of the National Academy of Sciences*, vol. 111, pp. 9733–9738, jun 2014.

[13] E. Ben-Jacob, O. Shochet, I. Cohen, A. Tenenbaum, A. Czirók, and T. Vicsek, "Cooperative strategies in formation of complex bacteria patterns," *Fractals*, vol. 03, pp. 849–868, dec 1995.

[14] C. W. Reynolds, "Flocks, herds and schools: A distributed behavioral model," in *Proceedings of the 14th annual conference on Computer graphics and interactive techniques - SIGGRAPH '87*, Association for Computing Machinery (ACM), 1987.

[15] G. Baglietto and E. V. Albano, "Nature of the order-disorder transition in the vicsek model for the collective motion of self-propelled particles," *Phys. Rev. E*, vol. 80, p. 050103, Nov 2009.

[16] G. Grégoire and H. Chaté, "Onset of collective and cohesive motion," *Phys. Rev. Lett.*, vol. 92, p. 025702, Jan 2004.

[17] H. Chaté, F. Ginelli, G. Grégoire, and F. Raynaud, "Collective motion of self-propelled particles interacting without cohesion," *Phys. Rev. E*, vol. 77, p. 046113, Apr 2008.

[18] H. P. Zhang, A. Be'er, E.-L. Florin, and H. L. Swinney, "Collective motion and density fluctuations in bacterial colonies," *Proceedings of the National Academy of Sciences*, vol. 107, no. 31, pp. 13626–13630, 2010.

[19] V. Narayan, S. Ramaswamy, and N. Menon, "Long-lived giant number fluctuations in a swarming granular nematic," *Science*, vol. 317, no. 5834, pp. 105–108, 2007.

[20] E. Lushi, H. Wioland, and R. E. Goldstein, "Fluid flows created by swimming bacteria drive self-organization in confined suspensions," *Proceedings of the National Academy of Sciences*, vol. 111, no. 27, pp. 9733–9738, 2014.

[21] M. Ballerini, N. Cabibbo, R. Candelier, A. Cavagna, E. Cisbani, I. Giardina, V. Lecomte, A. Orlandi, G. Parisi, A. Procaccini, M. Viale, and V. Zdravkovic, "Interaction ruling animal collective behavior depends on topological rather than metric distance: Evidence from a field study," *Proceedings of the National Academy of Sciences*, vol. 105, no. 4, pp. 1232–1237, 2008.

[22] D. J. G. Pearce, A. M. Miller, G. Rowlands, and M. S. Turner, "Role of projection in the control of bird flocks," *Proceedings of the National Academy of Sciences*, vol. 111, no. 29, pp. 10422–10426, 2014.

[23] F. Peruani, A. Deutsch, and M. Bär, "A mean-field theory for self-propelled particles interacting by velocity alignment mechanisms," *The European Physical Journal Special Topics*, vol. 157, no. 1, pp. 111–122, 2008.

[24] J. Gautrais, C. Jost, M. Soria, A. Campo, S. Motsch, R. Fournier, S. Blanco, and G. Theraulaz, "Analyzing fish movement as a persistent turning walker," *Journal of Mathematical Biology*, vol. 58, no. 3, pp. 429–445, 2009.

[25] P. Degond and S. Motsch, "Large scale dynamics of the persistent turning walker model of fish behavior," *Journal of Statistical Physics*, vol. 131, no. 6, pp. 989–1021, 2008.

[26] A. Campa, T. Dauxois, and S. Ruffo, "Statistical mechanics and dynamics of solvable models with long-range interactions," *Physics Reports*, vol. 480, no. 3–6, pp. 57 – 159, 2009.

[27] G. Falasco, "Role of long-range interactions in collective motion." Master Thesis, 2012.

[28] S. Benenti, "A "user-friendly" approach to the dynamical equations of non-holonomic systems," *Symmetry, Integrability and Geometry: Methods and Applications*, mar 2007.

[29] F. J. Segerer, F. Thüroff, A. Piera Alberola, E. Frey, and J. O. Rädler, "Emergence and persistence of collective cell migration on small circular micropatterns," *Phys. Rev. Lett.*, vol. 114, p. 228102, Jun 2015.